NASA TECHNICAL NOTE

NASA TN D-7959

A MONTE CARLO ANALYSIS OF THE VIKING LANDER DYNAMICS AT TOUCHDOWN

Ralph J. Muraca, Janet W. Campbell, and C. Anderson King

Langley Research Center
Hampton, Va. 23665

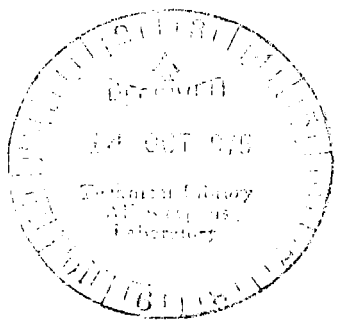

NATIONAL AERONAUTICS AND SPACE ADMINISTRATION • WASHINGTON, D. C. • SEPTEMBER 1975

1. Report No.	2. Government Accession No.	3. Recipient's Catalog No.
NASA TN D-7959		

4. Title and Subtitle	5. Report Date
A MONTE CARLO ANALYSIS OF THE VIKING LANDER DYNAMICS AT TOUCHDOWN	September 1975
	6. Performing Organization Code

7. Author(s)	8. Performing Organization Report No.
Ralph J. Muraca, Janet W. Campbell, and C. Anderson King	L-9830
	10. Work Unit No. 815-20-01-00

9. Performing Organization Name and Address	11. Contract or Grant No.
NASA Langley Research Center Hampton, Va. 23665	
	13. Type of Report and Period Covered
12. Sponsoring Agency Name and Address	Technical Note
National Aeronautics and Space Administration Washington, D.C. 20546	14. Sponsoring Agency Code

15. Supplementary Notes

C. Anderson King is an employee of Hampton Technical Center, LTV Aerospace Corporation, Hampton, Va.

16. Abstract

A dynamic computational analysis has been performed to determine the Viking lander motions, accelerations, leg forces, and body-ground clearances during and following the landing event. The performance of the Viking lander has been evaluated by using a Monte Carlo simulation, and all results are presented in statistical form. The primary objectives of this analysis were as follows:

(1) To determine the "three-sigma" design values of maximum rigid-body accelerations and the minimum clearance of the lander body during landing

(2) To determine the probability of an unstable landing

(3) To determine the probability of the lander body striking a rock

Two configurations were analyzed with the only difference being in the ability of the primary landing-gear struts to carry tension loads.

17. Key Words (Suggested by Author(s))	18. Distribution Statement
Landing dynamics Planetary lander simulations Monte Carlo simulation	Unclassified – Unlimited Subject Category 39

19. Security Classif. (of this report)	20. Security Classif. (of this page)	21. No. of Pages	22. Price*
Unclassified	Unclassified	55	$4.25

*For sale by the National Technical Information Service, Springfield, Virginia 22161

A MONTE CARLO ANALYSIS OF THE VIKING LANDER DYNAMICS AT TOUCHDOWN

Ralph J. Muraca, Janet W. Campbell,
and C. Anderson King*
Langley Research Center

SUMMARY

An analytical investigation was conducted to assess the performance capability of the Viking lander during the landing event. As part of the investigation, an extensive statistical analysis of the Viking lander was conducted with its prime objective being threefold:

(1) To determine the "three-sigma" design values for the maximum accelerations and the minimum clearance of the lander body during landing

(2) To determine the probability of a landing being unstable

(3) To determine the probability of the lander body striking a rock

To establish these design values, a simulation was constructed which allowed the motion of the Viking lander to be calculated from start of deorbit until the lander was stationary on the Mars surface. This simulation was broken into two major events: the entry phase (from deorbit until the lander reached the landing surface) and the landing phase (from the initial contact with the Martian surface until all motion ceased). During the landing phase of the simulation, the forces acting on the lander were modeled in considerable detail. Two configurations of the Viking lander were analyzed, the only difference being in the ability of the primary landing-gear struts to carry tension loads. One configuration appeared to be significantly more stable than the other without suffering any loss of performance in other respects.

INTRODUCTION

The problem of soft landing a legged spacecraft of the Lunar Module LM-Surveyor-Viking category is complicated by the large number of constraints imposed on the lander and by the opposing requirements which must be reconciled in an optimum design. The three major requirements of a lander are that the loads (accelerations) and clearance be

---

*Hampton Technical Center, LTV Aerospace Corporation, Hampton, Va.

constrained within established limits, while providing adequate stability. This trio of opposing requirements forms the basis of a highly challenging design problem.

Of the other constraints considered in the present investigation, some are common to all soft landers, whereas others are uniquely associated with the Viking lander (hereinafter referred to as VL). Due to the nature of the Viking mission, a highly efficient lander structure is required to minimize both weight and volume. In addition, the lander must be designed such that contamination of Mars does not occur and alterations to the landing site are minimized. This imposes constraints on materials and fabrication techniques and on nominal touchdown conditions.

Superimposed on this problem is the fact that knowledge of the Martian environment ranges from limited to nonexistent. Important aspects of the landing environment, such as surface slopes and rock sizes, have been defined based upon data whose accuracy is uncertain. These uncertainties combined with the high probability of success required of the mission have led to a highly constrained design.

The philosophy upon which the VL design was based required that design values be established in a probabilistic rather than a deterministic sense. To establish these design values, a computer simulation was constructed which allowed the motion of the VL to be calculated from the start of deorbit until the lander was stationary on the Martian surface. The simulation was divided into two major phases, the entry and the landing, which could be treated separately. The attitudes, rates, velocities, and external forces experienced by the lander at the end of its entry phase were taken as initial conditions for the landing phase. In addition to the results from the first phase, values for those random variables associated with the Martian surface and the lander configuration were generated by using Monte Carlo techniques.

The data resulting from the landing simulation were analyzed by using a variety of statistical procedures depending on the nature of the variable under consideration. In most instances where the goal was determination of "three-sigma" values for a variable, the procedure consisted of determining the curve which best fit the cumulative frequency data associated with that variable. However, in the cases of lander stability and impact with rocks, more complex treatments were required.

This report presents a description of the total simulation with concentration on the landing phase, a detailed description of the data analysis, and summary results for evaluation of the landing-system performance. The entry phase is described only briefly as it is well documented elsewhere.

SYMBOLS

The measurements and calculations were made in U.S. Customary Units. Values are given in SI Units and, where useful, also in U.S. Units.

d	stability distance from center of gravity of lander to a vertical plane passing through two footpads
d_{min}	minimum stability distance during the landing event
$\bar{d}_{min}$	sample mean minimum stability distance
E_k	kinetic energy of lander
F,K	strut force and stiffness characteristics, respectively, in load-stroke relationships
H	minimum clearance
I_{XX},I_{YY},I_{ZZ}	principal moments of inertia about the body axes
Pr(Event A|Condition B)	probability that event A occurs given that condition B exists
R	radius of rock
R_I	radius of impact zone
r	radius of lander body at its lowest point
s	sample standard deviation
$s_{d,min}$	sample standard deviation of minimum stability distances
t	time
Δt	time-increment size
V	velocity vector

X,Y,Z	body coordinates
$\bar{x}$	sample mean
α	landing-surface slope, degrees
δ	secondary-strut stroke length
$\dot{\theta}$	pitch rate, radians/second (degrees/second)
λ	parameter specifying the amount of lower hemisphere of rock lying above ground
μ	coefficient of friction between footpad and landing surface
ψ	roll angle, radians (degrees)

Subscript:

o	reference point

Abbreviations:

LMCP	Lander Monte Carlo Program
MEM	Mars Engineering Model
RNG	random-number generator

VIKING LANDER CONFIGURATION

Geometric and Mass Properties

A sketch of the VL is shown in figure 1. The lander is composed of a relatively rigid center structure to which three leg systems are attached. The center structure provides a mounting platform for the various scientific instruments and lander subsystems. Each leg system is composed of three struts.

Figure 2 shows a schematic drawing of the lander configuration with only the center body, legs, and footpads. Each leg consists of three struts in an inverted tripod arrangement with a footpad attached at the junction of the struts. The primary strut, also known as the upper or main strut, is attached to the body by a universal joint and contains a honeycomb shock absorber as an integral part of the design. Each secondary strut is attached by a universal joint to a load limiter which is attached to the body. The function of the load limiter is to limit the magnitude of the forces which can be transmitted to the lander body through the secondary struts. The limiters are designed to yield when the applied force exceeds a predetermined value. Thus, the limiters also act as energy absorbers.

Figure 3 defines the geometric relationship of the leg-strut attachment points and the footpad junction (shown as + symbols) relative to the center of gravity of the lander. The mass properties of the lander are also listed in this figure. The ratio of the center-of-gravity height above the surface to the footpad radius with the struts in an undeformed position is 0.566.

Function of Landing Leg System

Primary strut.- The primary strut contains an energy-absorption system composed of a crushable honeycomb cartridge which serves two functions: to reduce the forces acting on the center body and to absorb part of the kinetic energy of the lander. The honeycomb has one end tapered so that the force required to initiate crushing is less than the final force level. The strut loads elastically until the initial crush level is reached. The primary-strut load-stroke characteristics are shown in figure 4. Since crushing of the honeycomb creates permanent shortening, if extension of the strut occurs, there exists a region, called the deadband, where the strut has no load-carrying capability. In an attempt to eliminate the deadband region, the honeycomb is bonded to the strut so that the strut has some tensile load-carrying capability. However, a small deadband region exists in the current Viking lander strut.

Secondary struts.- The design used to limit the forces transmitted through the secondary struts is entirely different from that used in the primary struts. Figure 5 shows a schematic drawing of a secondary strut and its limiter. The limiter acts as a cantilever beam attached to the lander body. As loads are applied to the secondary strut, they cause the load limiter to bend. (See fig. 5.) The bending deformation is initially elastic but becomes plastic as the loads increase and the yield strength of the material is exceeded (approximately point 1). As the load on a limiter decreases from point 2, it returns to a new equilibrium position, point 3, due to the plastic deformation which has occurred. If the load reverses, the procedure is repeated but in the reverse direction. This is shown

in figure 5 by the dashed line and points 4 and 5. The entire cycle can be repeated if a compressive load is reapplied to the limiter, shown by points 6 and 7.

Engine Thrust Tailoff

The landing system is designed such that contact of any footpad with the surface initiates a signal to the lander propulsion system causing all three engines to shut down. (See fig. 6.) The delay between signal initiation t_1 and actual engine shutdown t_2 is a function of the propulsion-system design and the thrust decay once propellant flow has stopped. The thrust levels for each engine are individually controlled as part of the lander-attitude control system.

ENTRY PHASE

The entry phase of the simulation began with deorbit and ended when the center of gravity of the lander reached a point 1.397 meters (55 in.) above the surface. The entry phase utilizes a point-mass trajectory calculation until the time of terminal engine ignition and a six-degree-of-freedom calculation from that point.

Some of the features that were included in this phase were finite-burn deorbit maneuver, complete simulation of the Guidance and Control Sequencing Computer Flight equations during terminal descent, detailed relay link performance computations, and statistical atmospheres. The variables considered as random quantities in this simulation include orbit state, separation impulse, deorbit execution, roll attitude, trim angle of attack, atmosphere, aerodynamic coefficients, altimeter measurements, terrain height, parachute staging, parachute sway, long-term surface slopes, navigator attitude estimate, thrust misalinement, center-of-gravity location, engine specific impulse, winds, thrust calibration, terminal descent landing radar measurements, and tank pressure. Values for these quantities were generated by using Monte Carlo techniques which assumed appropriate distributions for the variables.

At the conclusion of each entry simulation, the following quantities were recorded for use as input to the landing phase:

(1) The VL attitude in the form of a transformation matrix

(2) The rigid-body translational velocities

(3) The rigid-body rotational rates

(4) Engine thrust levels

(5) Aerodynamic forces and moments

The entry phase was simulated 100 times by using three model atmospheres representing minimum, mean, and maximum atmospheric densities at the surface. Means and standard deviations for four of the five quantities listed are presented in table I for each of the three atmospheric models used. Examination of these data shows that the means and standard deviations do not vary greatly with the atmospheric model. The aerodynamic forces and moments exhibit the greatest variation with the maximum surface density producing the largest values. Therefore, the results from the 100 trajectories using the maximum surface density were used for the landing phase of the simulation.

LANDING PHASE

The landing phase of the simulation, beginning at the termination of entry (1.397 meters (55 in.) above the surface) and concluding when all motion has essentially stopped, considers the interaction between the lander and a rigid Martian surface as well as the effects of aerodynamic forces and descent engine thrust forces. In addition to the initial conditions obtained from the entry phase, other variables associated with the landing surface and the landing system had to be defined. Values for these other variables were obtained by using standard Monte Carlo techniques.

Lander performance was then measured in terms of the accelerations experienced during the landing, the available clearance following a landing, and the tendency for the lander to tip over during the landing. Other quantities which impact the lander-system design, such as primary and secondary strut loads (both tension and compression) and strokes, were also examined.

Simulation Description

The analysis of the motion of the VL during the landing phase of the simulation required integration of six equations describing the translational and rotational degrees of freedom of the lander.

The idealized VL, as depicted in figure 2, was assumed to consist of a rigid center body with three legs attached to it. All of the mass was assumed to be concentrated at the center of gravity, and the moments of inertia about each axis included the contribution of the legs. The external forces and moments which acted on the lander were caused by impact between the footpads and the Martian surface. These loads were transmitted through the leg struts and applied to the rigid lander body. Each of the struts experienced either elastic or plastic deformation in the axial direction; however, no transverse or torsional loads were transmitted through the struts.

The forces resulting when the lander contacted the surface were determined through a static analysis. The footpads were allowed to move with respect to the center body, and

their locations were determined by requiring that the entire system be in equilibrium at each time step. A detailed description of this procedure is included in the appendix. Also included in this appendix is a detailed description of the modeling used to simulate the action of the primary-strut energy absorber and the secondary-strut load limiters.

In an effort to minimize computation time without introducing unacceptable integration errors, a study was performed to determine the effect of integration step size on kinetic energy and rotation rates at a specified time during the landing event. The results of this effort are also included in the appendix.

The accuracy of the landing-phase analysis was demonstrated by comparing its results with those from a test program involving a dynamically scaled model of an earlier lander configuration. The primary objective of this study was to gain confidence in the ability of the analysis to predict loads, accelerations, and stability of the VL. A detailed discussion of this effort is contained in reference 1.

Input Parameters and Measurements

The mean and "three-sigma" values used as inputs to the landing simulations are given in table II. Those identified in the "Source" column as being from the LMCP (Lander Monte Carlo Program) are results of the 100 entry simulations using the atmosphere model with maximum surface density. In addition, other random inputs provided by a random-number generator at the start of the landing phase are indicated by RNG in the "Source" column.

The time delay associated with the shutdown signal to the terminal descent engine was assumed to be normally distributed with mean and "three-sigma" values given in table II. The surface slope distribution was obtained from the Mars Engineering Model (MEM), and the orientation of the slope with respect to the lander was assumed to be uniformly distributed between 0 and 2π radians. It was determined that a "three-sigma" dispersion of 10 percent of the nominal value could occur in the material properties of the shock absorbers and load limiters due to manufacturing variations. Consequently, these potential variations were incorporated into the model by using a random-number generator to assign their force levels.

Because of large uncertainties in defining the friction coefficient between the footpads and the Martian surface, it was decided that two complete sets of 100 landings would be simulated with all conditions identical except for the friction coefficient. The friction-coefficient values of 0.2 and 1.0 used for these two sets are believed to span the range of values likely to occur.

The quantities which best describe the performance of the VL and which were computed as part of each landing are given as follows:

(1) Clearance – This is defined as the distance between the landing surface and one of four reference points located in a reference plane on the underside of the lander body.

(2) Accelerations – These were vector magnitudes of the accelerations at the lander center of gravity and at six locations around the periphery of the lander body.

(3) Strut loads – These were the tension and compression loads in each strut.

(4) Strut strokes – These were the amounts of compression and extension stroking experienced by any of the struts.

(5) Stability distance – This was a quantitative measure of the lander stability. A more detailed explanation is presented in the following section.

To determine sample values for each of these parameters, all values during a given landing were surveyed and the maximum (or minimum) was selected. In the case of clearance, the minimum clearance of the four reference points was selected. For the off-body accelerations, the maximum acceleration of the six reference points was selected. Struts were divided into two categories, primary and secondary, and maximum tension and compression loads and strokes for each category were obtained.

Stability.- Little insight could be acquired concerning the stability characteristics of the lander using 100 landings onto random slopes. To observe the lander under marginally stable and unstable conditions, five slopes were selected ranging from 9^{o} to 35^{o}, and 50 simulations were made onto each of these slopes.

To provide quantitative information regarding the relative stability of different landings, a stability parameter was defined which gave a continuous measure of the stability of the lander at any instant. This parameter, called the stability distance d, was defined as the distance between the center of gravity of the lander and a plane parallel to the gravity vector passing through two footpads. Since the lander has three legs, there were three such planes or "stability walls." If the center of gravity of the lander was within the enclosure that was formed by the three stability walls, its gravity vector had a stabilizing effect on the lander dynamics. If the center of gravity was outside this enclosure, the gravity vector had a destabilizing effect and the landing was considered to be unstable.

To monitor the stability of the lander, the three stability distances were calculated for each time interval. By recording the minimum stability distance d_{min} which occurred during each landing, a relative measure of the stability of that landing could be obtained. If d_{min} became negative (the center of gravity passed through a stability wall), the lander was declared to be unstable. If d_{min} remained positive and the kinetic energy of the lander diminished to less than 0.5 percent of the average kinetic energy at impact, the landing was declared stable and the simulation was terminated.

Locations for monitoring stability, acceleration, and clearance.- Figure 7 shows the locations for the monitors that were used to determine the accelerations, clearances, and stability distances. The six "accelerometers" were equally spaced around the circumference of a circle lying in the plane of the center of gravity that bounded all the major engineering and scientific equipment. The four clearance monitors were located in a plane passing through the lowest point on the lander body. One point was located directly on the symmetric axis of the lander, and the other three points were equally spaced on a circle about a symmetric axis.

STATISTICAL ANALYSIS OF THE LANDING EVENT

Introduction

Once the simulations were complete, the statistical behavior of the resultant landing parameters was analyzed. This analysis sought to answer the following three basic questions:

(1) What are the "three-sigma" design values for the maximum rigid-body acceleration, minimum clearances, and maximum compression and tension strut forces and strokes?

(2) What is the probability that the lander will become unstable as a result of landing on a steep slope?

(3) What is the probability that the body of the lander will strike a rock?

The adjective "three sigma" in question (1) is used to refer to a value which is exceeded with probability 0.0013. If the probability distribution of the parameter is Gaussian, then this design value would, in fact, be three standard deviations (three sigma's) away from its mean. Since distributions are not, in general, Gaussian (e.g., some are skewed rather than symmetrical), these 0.0013-probability design values are not necessarily three standard deviations from their means. Hence, quotation marks are used around "three sigma."

In order to give a specific numerical answer to questions (2) and (3), it was necessary to assume distributions for surface slopes and rock sizes on Mars. Estimates of the distributions used in this analysis were those prescribed in the Mars Engineering Model. Because of the speculative nature of these distributions (e.g., rock distributions are based on Lunar rock distributions), this study was designed so as to decouple the actual landing simulations from the assumed slope or rock distributions. For example, to answer the question of stability, Monte Carlo simulations were used to estimate the probability of instability when landing on a particular slope α for different values of α. This probability, independent of the slope distribution, was then combined analytically with the

prescribed slope distribution to give the overall probability of instability as an answer to question (2). To determine the probability of striking a rock, landings on a low friction (μ = 0.2) rock-free surface were simulated, and the distribution of minimum clearances was obtained. This minimum-clearance distribution, independent of any rock distribution, was then combined analytically with the assumed distribution of rock sizes to answer question (3).

One advantage of this approach was that expensive computer simulations need not be repeated if the rock and/or slope distributions are modified. Furthermore, parameters in the rock and slope distributions could be varied to determine the sensitivity of the present results to possible errors in these underlying distributions.

Determination of Design Values

The twelve parameters which were tabulated for each landing event are given as follows:

(1) Minimum stability distance

(2) Minimum clearance

(3) Maximum acceleration at the center of gravity

(4) Maximum acceleration at the "accelerometers"

(5) Maximum primary-strut compressive force

(6) Maximum primary-strut tensile force

(7) Maximum secondary-strut compressive force

(8) Maximum secondary-strut tensile force

(9) Maximum primary-strut compressive stroke

(10) Maximum primary-strut tensile stroke

(11) Maximum secondary-strut compressive stroke

(12) Maximum secondary-strut tensile stroke

The design values for these parameters were based on either the high-friction sample or the low-friction sample, depending on whether high or low friction was more critical. This choice adds a degree of conservatism to the design values, but it appears to be unavoidable when considering the present lack of knowledge of surface friction.

Figure 8 illustrates the type of information used to obtain design values for each parameter. It lists the mean, standard deviation, and first four moments of the minimum clearances together with their histogram and cumulative-frequency plots.

Three different methods were used in estimating design values for each parameter. According to the first method, which is perhaps the most common approach, the parameter distribution was assumed to be Gaussian, and the design value was taken to be $\bar{x} \pm 3s$ where $\bar{x}$ was the sample mean and s the sample standard deviation. A plus or minus sign was chosen depending on whether the design value was a maximum or minimum, respectively.

With the second method, it was again assumed that the parameter had a Gaussian distribution. A theoretical Gaussian cumulative-frequency curve was fitted to the observed cumulative frequency by obtaining a linear least-squares fit on Gaussian probability paper. Once this fit was made, the parameter value corresponding to an exceedance probability of 0.0013 was chosen. This also produced a value which was literally three standard deviations from the mean, although the estimates of population mean and standard deviation were not the same as $\bar{x}$ and s.

The third method did not assume a Gaussian distribution. By using the first four sample moments, one of the generalized Pearson distributions (ref. 2) was fitted to the observed distribution. All probability distributions which can be defined by their first four moments were classified by Pearson into five generalized categories. This system includes virtually all well-known distributions such as Gaussian, Weibull, Gamma, Beta, Exponential, Chi-squared, and many others. By fitting a Pearson distribution to the data, the best possible fit to the observed distribution was found.

In the case of the symmetrical minimum-clearance histogram, there was little difference between the Gaussian fit (fig. 9(a)) and the Pearson type IV fit (fig. 9(b)). However, an example where the two methods were noticeably different was the histogram constructed from maximum center-of-gravity accelerations shown in figure 10. Since this histogram was skewed, a normal distribution could not be expected to provide a good fit. The Pearson type I distribution (fig. 10(b)) was a much better fit.

Table III lists 10 parameters and their design values obtained by the different methods. (Maximum primary-strut tensile stroke was omitted here because no tensile strokes occurred in the primary struts.) Values listed in this table under the heading "Sample extreme" were extremes which occurred in the sample of size 100. Where this value exceeds a design value (e.g., maximum primary-strut tensile force by methods 1 and 2), a poor design value is indicated. This is because extremes in a sample of size 100 should occur with a frequency of approximately 1 in 100 (exceedance probability of 0.01 instead of 0.0013). That is, extremes in these samples should lie approximately two standard deviations from their means.

In many cases, the three methods yielded design values in close agreement with one another, and, in these instances, there was no real need to choose one method over

the others. Nevertheless, if one were to make a choice, method 3 is recommended over the other two methods because it did not make the arbitrary assumption that the parameter distribution was Gaussian.

The entire simulation was repeated assuming a VL configuration in which the primary struts had infinite tensile load-carrying capability (no deadband) as would be the case if they were equipped with a ratchet. No appreciable difference was observed for any of the 10 parameters in table III.

Stability

To determine $\Pr(\text{Instability}|\text{Slope} = \alpha)$ as a function of α, the landing simulations onto discrete fixed slopes were used. According to the formulation of this problem, the probability of turning over was simply the probability that d_{min} became negative. That is,

$$\Pr(\text{Instability}|\text{Slope} = \alpha) = \Pr\left(d_{min} \leqq 0 \middle| \text{Slope} = \alpha\right)$$

Upon examination of the derived d_{min} distributions, shown in figure 11, it appeared that each distribution had two or three distinct clusters. A comparison of landing-phase initial conditions revealed that landings tended to have larger d_{min} values (i.e., were more stable) if one of the three legs was initially pointing approximately in the downhill direction. In effect, the clustering of d_{min} values was linked to the orientation of the legs relative to the landing-surface slope, a random input to the landing phase. Accordingly, the 50 landings at each slope were divided into three categories depending on the initial orientation of the legs relative to the downhill direction. These categories are listed as follows:

A. One leg pointing in the downhill direction ($\pm 15^{\circ}$)

B. One leg pointing in the uphill direction ($\pm 15^{\circ}$)

C. No leg pointing either uphill or downhill as defined in A and B

Landings in category A were called 2-1 landings because two legs strike the surface first almost simultaneously and then the third leg strikes. Similarly, landings in categories B and C were called 1-2 and 1-1-1 landings, respectively. Figure 12 shows how the histogram clusters in figure 11 were associated with these categories.

Because the orientation angle of the legs with respect to the slope was uniformly distributed, A and B landings were equally likely to occur, and C landings were twice as likely to occur. (See fig. 13.) That is, the aforementioned three landings should theoretically occur in porportions of 1:1:2, respectively.

The d_{min} values associated with a particular landing type, at a fixed α, were assumed to have Gaussian distributions. That is, each cluster shown in figure 12 represented a sample from a Gaussian population. The means and standard deviations of these samples were plotted as functions of α (fig. 14). The following relationships were determined by the least-squares method:

Type A (2-1) landings:

$$\bar{d}_{min} = 25.73 - 0.1092\alpha - 0.00991\alpha^2$$

$$s_{d,min} = -0.1205 + 0.0732\alpha$$

Type B (1-2) landings:

$$\bar{d}_{min} = 28.90 - 0.7273\alpha - 0.00645\alpha^2$$

$$s_{d,min} = 0.5483 + 0.0586\alpha$$

Type C (1-1-1) landings:

$$\bar{d}_{min} = 28.15 - 0.5937\alpha - 0.00556\alpha^2$$

$$s_{d,min} = 0.5617 + 0.0783\alpha$$

where $\bar{d}_{min}$ and $s_{d,min}$ are the mean and standard deviations of d_{min}, respectively.

With the previously stated assumptions about the d_{min} distributions, it is possible to estimate the probability of turning over when landing on a slope α for each of the three landing types. By denoting these probabilities as $\Pr\left(d_{min} \leqq 0 \middle| \alpha;A\right)$, $\Pr\left(d_{min} \leqq 0 \middle| \alpha;B\right)$, and $\Pr\left(d_{min} \leqq 0 \middle| \alpha;C\right)$, then for any general landing the probability of turning over, given the slope α, is

$$\Pr\left(d_{min} \leqq 0 \middle| \text{Slope} = \alpha\right) = \frac{1}{4}\Pr\left(d_{min} \leqq 0 \middle| \alpha;A\right) + \frac{1}{4}\Pr\left(d_{min} \leqq 0 \middle| \alpha;B\right) + \frac{1}{2}\Pr\left(d_{min} \leqq 0 \middle| \alpha;C\right)$$

(This probability is a weighted sum based on the relative proportions of the three landing types.)

The three broken curves in figure 15 are plots of $\Pr\left(d_{min} \leqq 0 \middle| \alpha;A\right)$, $\Pr\left(d_{min} \leqq 0 \middle| \alpha;B\right)$, and $\Pr\left(d_{min} \leqq 0 \middle| \alpha;C\right)$ against α, and the solid curve is their weighted sum $\Pr\left(d_{min} \leqq 0 \middle| \text{Slope} = \alpha\right)$.

By returning to the d_{min} distributions for the different slopes, and by placing statistical bounds on the amount of error which might have occurred as a result of small sample sizes, it was possible to calculate an error envelope for the probability curves in figure 15. These upper and lower limits, the dashed curves in figure 16, represent bounds within which the true probability curve, $\Pr\left(d_{min} \leq 0 \middle| \text{Slope} = \alpha\right)$ against α, should lie.

The probability curves in figures 15 and 16 were independent of the slope distribution. For example, the probability of turning over when landing on a 45° slope was estimated as 0.85, but no indication was given as to the probability of encountering such a steep slope. Figure 17 is a plot of the slope distribution (i.e., the probability that the slope is greater than α as a function of α) as given in the Mars Engineering Model. According to this reference, the slopes have an exponential distribution with 90 percent of all slopes being less than 11.7°. Combining this slope distribution with the probability curve $\Pr\left(d_{min} \leq 0 \middle| \text{Slope} = \alpha\right)$ and integrating over α gave the answer to question (2) as follows:

> The probability that the Viking lander will become unstable as a result of landing on a steep slope is 0.0012.

In order to determine the sensitivity of this probability estimate to the choice of 11.7° as the 90th percentile slope, the latter was varied to give the curve in figure 18. The current probability estimate (0.0012) corresponding to a 90th percentile slope of 11.7° is indicated by the star. This plot shows the relative sensitivity of the aforementioned answer to the choice of slope distribution. For example, if the 90th percentile slope were as high as 15°, the probability of instability would be 0.0047, almost four times greater than the present estimate. The upper and lower limits in figure 16 yield the bounds (broken curves) in figure 18. From this, it is possible to state that the probability of instability based on the current slope distribution in the Mars Engineering Model is between 0.0008 and 0.0017.

The entire analysis was repeated by using the simulations for a modified lander configuration (no deadband) as discussed previously. The resulting curve of $\Pr\left(d_{min} \leq 0 \middle| \text{Slope} = \alpha\right)$ against α is shown in figure 19 with its upper and lower limits, and the corresponding curve of Pr(Instability) against the 90th percentile slope is shown in figure 20. The modified design decreased the probability of turning over by 25 percent, that is, from 0.0012 to 0.0009.

Striking a Rock

By using the sample of 100 minimum clearances associated with low-friction landings, the histogram of figure 21 was obtained. The dashed curve is a theoretical

probability function (Pearson type IV) which was fitted to the minimum-clearance frequencies. This theoretical distribution, combined with the rock distributions in the Mars Engineering Model, was used to estimate the probability of striking a rock.

The rock distributions, based on Lunar Surveyor photographs, were expressed in terms of the proportion of area covered by rocks with radii greater than R. In the present study, rocks were modeled as spheres embedded in the planet surface anywhere from 0 to 50 percent. (See fig. 22.) Actually, if a rock were embedded more than 50 percent, the area covered by that rock would be perceived by an overhead camera as the area covered by a rock of radius R' (see fig. 22(d)); and, hence, the rock would have been accounted for in the rock distributions as a smaller rock.

An important consideration was the amount by which a rock was embedded before deciding whether the lander could strike that rock. For example, let H denote a value of minimum clearance measured for a particular landing, and assume that this landing was made directly on top of a rock of diameter H. The rock will touch the lower surface of the lander only if the rock is totally above ground as shown in figure 23(a).

Two extreme cases were considered in the present analysis to define upper and lower limits on the probability of striking a rock. The first case, which assumed that all rocks were submerged 50 percent, gave a lower bound for the probability of striking a rock. The second case, giving an upper bound, assumed that all rocks were totally above ground.

For each rock large enough to strike the lander, an impact zone was defined such that if the center of gravity of the lander were within this zone, the lander would strike that rock. Figure 23 illustrates how the radii R_I of the impact zones were defined for the two extreme cases studied.

The rock area distributions in the Mars Engineering Model, based on Surveyor III, V, and VI data, gave the proportion of surface area covered by rocks of radii greater than R as a function of R. By using these distributions, it was possible to calculate the proportion of the total Mars surface area covered by potential impact zones for any landing with a specific minimum clearance H. Mathematically, this proportion is equivalent to the probability of striking a rock when the minimum clearance is equal to H, denoted as Pr(Strike rock|Minimum clearance = H). Plots of Pr(Strike rock|Minimum clearance = H) against H are shown in figure 24(a) for the embedded-rock case and in figure 24(b) for the unembedded-rock case, respectively. The three curves in each figure are for the three rock distributions of Surveyor III, V, and VI.

These probability curves are independent of the distribution of minimum clearance H (fig. 21) which was estimated from the Monte Carlo simulations. By combining

the distribution of H with the Pr(Strike rock|Minimum clearance = H) and integrating over H, upper and lower bounds for the answer to question (3) were obtained as follows:

> The probability that the body of the lander will strike a rock is between 0.006 and 0.025 if landing at a relatively rocky site, such as that of Surveyor III, and between 0.001 and 0.005 if landing at a relatively smooth site, such as that of Surveyor V.

By assuming that the embedding is purely random such that the probability of a rock being embedded, say, 30 percent, is equal to the probability of its being embedded any other percentage between 0 and 50 percent, then a specific answer to question (3) can be obtained.

Let λ be a parameter (as defined in fig. 25) which specifies the fraction of the lower hemisphere of the rock lying above the ground. Then, by using the general equation for the radius of an impact zone

$$R_I = \begin{cases} r + \sqrt{R^2 - (H - \lambda R)^2} & (H/(\lambda + 1) \leqq R < H/\lambda) \\ r_o + R & (H/\lambda \leqq R) \end{cases}$$

it is possible to calculate the probability of striking a rock for a particular λ. (See fig. 26.) Finally, by integrating this probability from $\lambda = 0$ (50 percent embedding) to $\lambda = 1$ (no embedding), the specific answer to question (3) became:

> The probability that the body of the lander will strike a rock is 0.016 if landing at a relatively rocky site, such as that of Surveyor III, and 0.003 if landing at a relatively smooth site, such as that of Surveyor V.

DISCUSSION OF RESULTS

As previously stated, the design of a soft lander is influenced by three primary requirements: to minimize landing shocks, to provide adequate clearance above the landing surface, and to provide adequate stability. In the case of the VL, these constraints were quantified as follows: The "three-sigma" acceleration at any point located on a circle with radius of 106.68 cm (3.5 ft) must not exceed 14.12 g units or 30 g units if including a safety factor (1.25) and dynamic effects (1.7). The "three-sigma" value of minimum clearance must exceed 22 cm (8.66 in.), and the lander must be stable over 99 percent of the time when landing in a region where 90 percent of the slopes are less than 11.7°. In meeting these requirements, the landing system was also required to limit primary-strut stroking to less than 27.9 cm (11 in.).

The results from this simulation are summarized in table III. The "three-sigma" rigid-body acceleration is 13.96 g units; and when dynamic effects and a safety factor are included, this value becomes 29.7 g units. The constraint on minimum clearance has been met by the simulated VL which had a "three-sigma" value for minimum clearance of 29.31 cm (11.54 in.). In the simulation, the configuration was stable 99.88 percent of the time, and the "three-sigma" value of primary-strut compression stroke was 12.57 cm (4.95 in.).

The secondary struts exhibit a highly nonlinear behavior when the stroke exceeds about 7.62 cm (3 in.); consequently, this was established as the allowable value. This limit is less than the "three-sigma" value of 8.59 cm (3.38 in.) obtained in the simulation. Although a minimum allowable clearance has been established for the VL design, no success criteria has ever been established with respect to the lander body striking a rock. Consequently, no comparison with a design "three-sigma" value is possible for this parameter. The simulation results indicate that the probability of striking a rock is between 0.003 and 0.016 depending on the assumed rock distributions.

The simulation results indicate that the "three-sigma" values for the parameters considered are within the capability of the VL design. Equipping the VL with a ratchet on each primary strut capable of withstanding tensile loading improved stability without significantly affecting other parameters.

The discrepancies associated with modeling the landing surface as a rigid nonyielding plane as opposed to a contoured, deformable map cannot be assessed. Intuition would lead one to predict that a deformable, energy-dissipating surface would reduce loads, decrease clearance, and improve stability. However, as with most complex systems having a large number of variables, the use of intuition can lead to incorrect conclusions. The effect of including center-body elasticity in the analysis is likewise unknown. Some indication can be obtained by comparing these data with the results in reference 3. However, any extrapolation beyond the test configuration and conditions should be made with caution.

CONCLUDING REMARKS

The Viking lander (VL) design, as analyzed in the present Monte Carlo study, is capable of adequately meeting all established design criteria. In cases where design criteria have not been established, the "three-sigma" variability in these parameters demonstrated in the simulations was well within the capability of the actual VL design. The probability of becoming unstable as a result of landing on a very steep slope was estimated to be 0.0012, and the probability of striking a rock was estimated to be between 0.003 and 0.016 depending on the assumed rock distribution at the selected landing site.

The "three-sigma" value of rigid-body acceleration on a circle of radius 1.0668 meters (3.5 ft) is 13.96 g units.

Equipping the VL with a ratchet on each primary strut capable of withstanding any tensile loading improved stability without significantly affecting other parameters.

Langley Research Center
National Aeronautics and Space Administration
Hampton, Va. 23665
June 6, 1975

APPENDIX

LANDING DYNAMICS COMPUTER PROGRAM

Model Description

The landing dynamic model used to simulate the landing event was the Landing Dynamics Computer Program (LDCP). The idealized lander was assumed to have a rigid body with three massless legs attached. (See fig. 2.) The LDCP simulates the dynamic behavior of the lander by considering the rigid body as having six degrees of freedom and numerically integrating the respective equations of motion.

Mass and Inertias

The inertial properties of the body were characterized by specification of the total mass, the center of gravity, a set of principal axes, and the moments of inertia taken about the principal axes. In representing an actual vehicle, the inertial properties were computed for the system as a whole, including the legs. These inertial properties were then assigned to the body alone in the idealized system.

Shock Absorbers

In the idealized system, the strut forces were assumed to act along the instantaneous axis of the strut. The magnitude of the shock-absorber force was a function of the strut stroke which was defined to be the change in length of the strut from its initial length. The force-stroke relationships for the primary and secondary struts, respectively, are described subsequently.

Primary struts.- The shock-absorber force-stroke relationship for the primary strut consisted of four discrete force levels and associated stroke lengths, as shown in figure 27. A description of a typical force-stroke history follows. Initially, the strut deformed elastically until the first force level was reached. At that point, a constant force level was maintained until the shock absorber experienced complete plastic deformation. As the load continued to increase, the shock absorber experienced a second elastic deformation until the next force level was reached. This procedure continued until the highest force level was reached. The strut unloaded elastically until zero force was reached. There were four options modeled in the LDCP for simulating the tensile capability of the strut. These options are listed as follows:

(1) The strut could go directly into tension elastically.

(2) Before the strut could go into tension, it reextended to its initial length. Hence, there existed a region called the deadband, where the strut had no load-carrying

capability. Once the strut had completely reextended, it then deformed elastically under a tension load.

(3) Before the strut could go into tension, it had to go through a limited specified deadband. Once the strut had passed through this limited deadband, it then deformed elastically under a tension load. An example of this option was a strut with a ratchet which prevented reextension.

(4) Before the strut could go into tension, it had to go through a limited specified deadband as in option (3). Once the strut had passed through this limited deadband, it had a limited tensile load-carrying capability. Once the limited tensile capability was exceeded, the strut force-stroke relationship was similar to that of option (2). An example of this option was a strut with its crushable honeycomb bonded to the strut.

Secondary struts.- The actual secondary-strut load limiter was designed to limit the load-transmitting capability of the strut by bending plastically. The effects of the load limiter were modeled by assuming that the flexural force-deflection relationship of the limiter could be replaced by an axial load-stroke relationship of the strut (fig. 28). The secondary-strut force-displacement relationship was modeled as having four ramps for both compression and tension forces. Along the first ramp, the strut was assumed to deform elastically. The other three ramps simulated the plastic region of the force-deflection relationship of the limiter. The unloading of the strut force was assumed to occur elastically regardless of the plastic deformation the limiter had experienced. If permanent deformation had occurred, the load-stroke curve was shifted so that no deadband existed. The load-stroke curve was modeled similarly for both the tension and compression forces. A given strut was allowed to have different stiffness characteristics in tension and compression.

Pad Motions

The basic assumption in calculating the motion of the individual pads was that at the completion of a time step, each pad junction was in static equilibrium under the action of the forces acting at the junction. If a pad was contacting the landing surface, these forces consisted of the axial forces in the three struts and the pad force. If a pad was free of the landing surface, these forces were absent and there was no relative motion between the body and the pad.

At the beginning of an iteration step, the body was allowed to move to a new position dictated by the acting forces and moments. If a pad was free of the landing surface, its new equilibrium position was determined by assuming the pad to be part of the rigid body. If the pad was contacting the landing surface, the strut forces were calculated with the body in the new position and the pad in its old position. The normal and tangential components of the resultant force of the three struts with respect to the landing surface were

calculated. If the normal component was directed into the surface, the pad was considered to be on the surface and an equivalent normal pad force was applied in the opposite direction. The tangential component of the resultant force was compared with the friction force. If the friction force, which is based on Coulomb friction, was greater than the tangential force, no movement of the pad was allowed since the friction force prohibited the pad from sliding along the surface. If the tangential force was greater than the friction force, the pad was allowed to slide along the landing surface until the friction force and the tangential force were in equilibrium. If the initial normal component of the resultant force was directed away from the landing surface, the pad was considered to be leaving the surface and no force existed in the struts.

Time-Interval Size

In order to determine the largest practical time-interval size for the numerical integration, several landings were simulated by using different time intervals for each landing. In order to evaluate the effects of the time-interval size, the kinetic energy, pitch rate, and velocity components of the lander at 0.4 second after initial touchdown were compared for each increment size. With the use of the smallest time increment, 10^{-5} second, as a reference, the ratios of these quantities are shown in figure 29. Upon examining this figure, a time interval of 10^{-4} second appears to be the largest practical size for use in these simulations.

REFERENCES

1. Muraca, Ralph J.; and King, C. Anderson: Verification of a Landing Dynamics Computer Program Using Viking Lander Data. NASA TM X-72653, 1975.

2. Kindall, Maurice G.; and Stuart, Alan: The Advanced Theory of Statistics. Volume 1 – Distribution Theory. Second ed. Hafner Pub. Co., c.1963.

3. McGehee, John R.; and Stubbs, Sandy M.: Experimental Validation of a Landing-Dynamics Computer Program for Legged Spacecraft Landers. NASA TN D-7301, 1973.

TABLE I.- MEANS AND STANDARD DEVIATIONS FOR INITIAL CONDITIONS OBTAINED FROM 100 TRAJECTORIES FOR THREE ATMOSPHERES

Quantity	Maximum density		Mean density		Minimum density	
	Mean	s	Mean	s	Mean	s
Engine thrust, N (lbf)						
Engine 1	756.6 (170.1)	20.5 (4.6)	756.2 (170.0)	19.6 (4.4)	754.4 (169.6)	19.6 (4.4)
Engine 2	642.8 (144.5)	20.0 (4.5)	642.8 (144.5)	19.6 (4.4)	641.9 (144.3)	19.6 (4.4)
Engine 3	751.7 (169.0)	19.1 (4.3)	751.3 (168.9)	19.1 (4.3)	750.0 (168.6)	18.7 (4.2)
Body angular rates, rad/s (deg/sec)						
Pitch	7.68×10^{-5} (0.0044)	3.26×10^{-4} (0.0187)	8.20×10^{-5} (0.0047)	3.54×10^{-4} (0.0203)	1.13×10^{-4} (0.0065)	4.03×10^{-4} (0.0231)
Yaw	3.67×10^{-5} (0.0021)	4.14×10^{-4} (0.0237)	3.67×10^{-5} (0.0021)	4.36×10^{-4} (0.0250)	3.49×10^{-5} (0.0020)	5.10×10^{-4} (0.0292)
Roll	-8.20×10^{-5} (-0.0047)	2.30×10^{-3} (0.1319)	2.97×10^{-5} (0.0017)	2.41×10^{-3} (0.1382)	-9.60×10^{-5} (-0.0055)	2.55×10^{-3} (0.1463)
Body velocity, mps (fps)						
X-axis	-0.0037 (-0.0120)	0.1042 (0.3417)	-0.0037 (-0.0122)	0.1048 (0.3437)	-0.0051 (-0.0168)	0.1063 (0.3489)
Y-axis	0.0553 (0.1815)	0.1351 (0.4434)	0.0543 (0.1781)	0.1351 (0.4432)	0.0528 (0.1731)	0.1351 (0.4434)
Z-axis	2.4257 (7.9583)	0.1320 (0.4331)	2.4322 (7.9797)	0.1316 (0.4318)	2.4388 (8.0012)	0.1313 (0.4308)
Aerodynamic forces, N (lbf)						
X-axis	-0.0538 (-0.0121)	19.1932 (4.3148)	0.0020 (0.0045)	13.4394 (3.0213)	0.0592 (0.0133)	10.0107 (2.2505)
Y-axis	2.8798 (0.6474)	16.4798 (3.7048)	1.8852 (0.4238)	11.6646 (2.6223)	1.2655 (0.2845)	8.7514 (1.9674)
Z-axis	6.4940 (1.4599)	5.0603 (1.1376)	4.3575 (0.9796)	3.1849 (0.7160)	3.1582 (0.7100)	2.2219 (0.4995)
Aerodynamic moments, N-m (lbf-ft)						
X-axis	-0.8270 (-0.6100)	5.1659 (3.8102)	-0.5182 (-0.3822)	3.3917 (2.5016)	-0.3384 (-0.2496)	2.4334 (1.7948)
Y-axis	0.1912 (0.1410)	5.7664 (4.2531)	0.1712 (0.1263)	3.7838 (2.7908)	0.1466 (0.1081)	2.7115 (1.9999)
Z-axis	0 (0)	0 (0)	0 (0)	0 (0)	0 (0)	0 (0)
Inertial velocity, mps (fps)						
Vertical	2.4255 (7.9576)	0.1322 (0.4338)	2.4321 (7.9793)	0.1318 (0.4323)	2.4387 (8.0010)	0.1314 (0.4311)
Horizontal	0.1607 (0.5272)	0.0862 (0.2828)	0.1589 (0.5212)	0.0859 (0.2817)	0.1584 (0.5198)	0.0864 (0.2834)

TABLE II.- MEANS AND THREE STANDARD DEVIATIONS OF INPUT DATA FOR THE LANDING DYNAMICS COMPUTER PROGRAM

Quantity	Mean ± 3s	Source
Velocity, mps (fps)		
Vertical	2.4255 ± 0.3966 (7.9576 ± 1.3014)	LMCP
Horizontal	0.1607 ± 0.2586 (0.5272 ± 0.8484)	LMCP
Body attitude, rad (deg)		
Pitch	0.0017 ± 0.0227 (0.1 ± 1.3)	LMCP
Yaw	0.0017 ± 0.0297 (0.1 ± 1.7)	LMCP
Roll	Uniform between 0 and 2π	LMCP
Body angular rates, rad/s (deg/sec)		
Pitch	$7.68 \times 10^{-5} \pm 9.79 \times 10^{-4}$ (0.0044 ± 0.0561)	LMCP
Yaw	$3.67 \times 10^{-5} \pm 1.241 \times 10^{-3}$ (0.0021 ± 0.0711)	LMCP
Roll	$-8.20 \times 10^{-5} \pm 6.90 \times 10^{-3}$ (-0.0047 ± 0.3957)	LMCP
Aerodynamic forces, N (lbf)		
X-axis	-0.0538 ± 57.5796 (-0.0121 ± 12.9444)	LMCP
Y-axis	2.8798 ± 49.4394 (0.6474 ± 11.1144)	LMCP
Z-axis	6.4940 ± 15.1809 (1.4599 ± 3.4128)	LMCP
Aerodynamic moments, N-m (lbf-ft)		
X-axis	-0.8270 ± 15.4978 (-0.6100 ± 11.4306)	LMCP
Y-axis	0.1912 ± 17.2992 (0.1410 ± 12.7593)	LMCP
Z-axis	0 ± 0 (0 ± 0)	LMCP
Engine thrust forces, N (lbf)		
Engine 1	756.6 ± 61.4 (170.1 ± 13.8)	LMCP
Engine 2	642.8 ● 60.1 (144.5 ● 13.5)	LMCP
Engine 3	751.7 ± 57.4 (169.0 ± 12.9)	LMCP
Engine thrust delay, sec	0.044 ± 0.016	RNG
Load-stroke perturbation factor		
Primary	1 ± 0.1	RNG
Secondary	1 ± 0.1	RNG
Surface, rad (deg)		
Slope	Exponential distribution with 90th percentile, 0.2042 (11.7)	RNG
Direction	Uniform between 0 and 2π	RNG

TABLE III.- DESIGN VALUES WITH "THREE-SIGMA" EXCEEDANCE PROBABILITY

Landing parameter	Sample extreme	Method 1 (sample statistics)	Method 2 (probability papers)	Method 3 (Pearson)
Low-friction landings				
Minimum clearance, cm (in.)	29.81 (11.736)	29.39 (11.571)	29.21 (11.5)	29.31 (11.539)
Maximum primary-strut compression force, N (lbf)	11 743 (2640)	11 832 (2660)	11 979 (2693)	11 694 (2629)
Maximum primary-strut compression stroke, cm (in.)	12.24 (4.820)	12.53 (4.935)	12.88 (5.070)	12.57 (4.950)
High-friction landings				
Maximum c.g. acceleration, Earth g units	7.04	7.64	7.74	6.91
Maximum accelerometers acceleration, Earth g units	13.91	14.30	14.81	13.96
Maximum primary-strut tension force, N (lbf)	975.04 (219.2)	361.9 (81.37)	398.1 (89.50)	1031.9 (232.0)
Maximum secondary-strut compression force, N (lbf)	8465 (1903)	8109.1 (1823)	8429.4 (1895)	8625.1 (1939)
Maximum secondary-strut tension force, N (lbf)	6467.7 (1454)	7971.2 (1792)	7450.8 (1675)	6249.8 (1405)
Maximum secondary-strut compressive stroke, cm (in.)	7.62 (3.00)	5.61 (2.21)	7.16 (2.82)	8.59 (3.38)
Maximum secondary-strut tensile stroke, cm (in.)	0.51 (0.202)	0.18 (0.070)	0.37 (0.146)	0.60 (0.238)

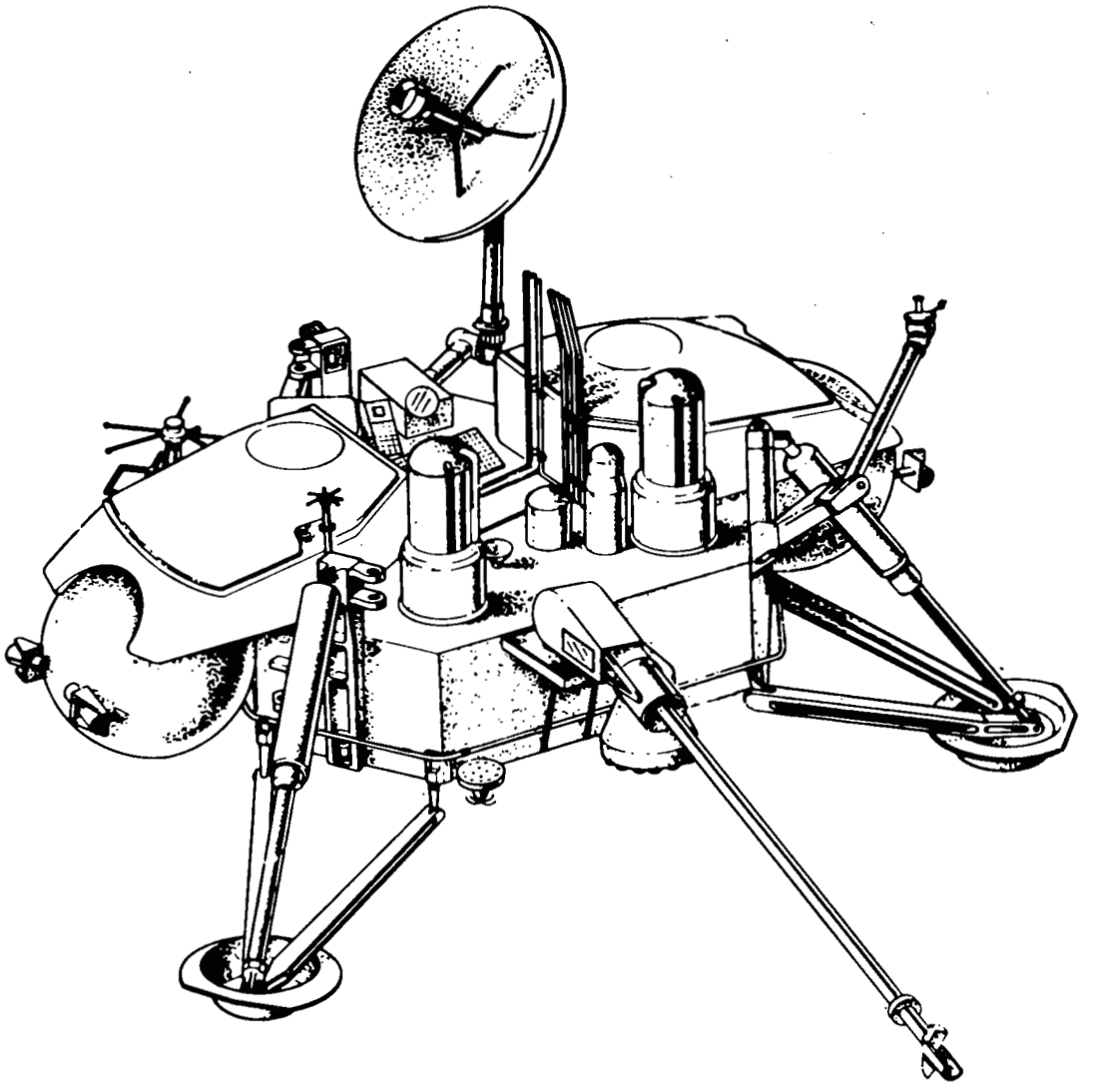

Figure 1.- Viking lander configuration.

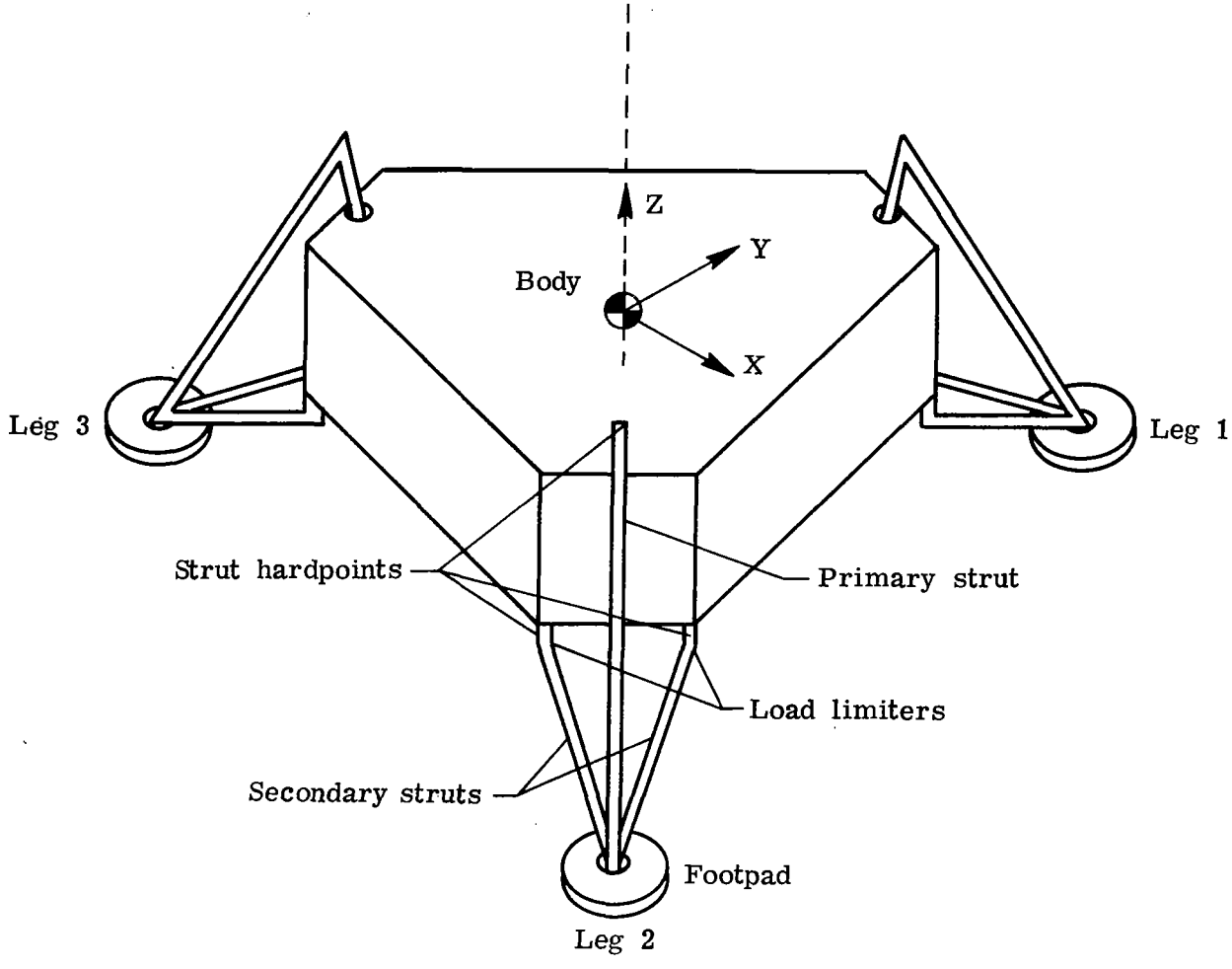

Figure 2.- Schematic drawing of the Viking lander center body, legs, and footpads.

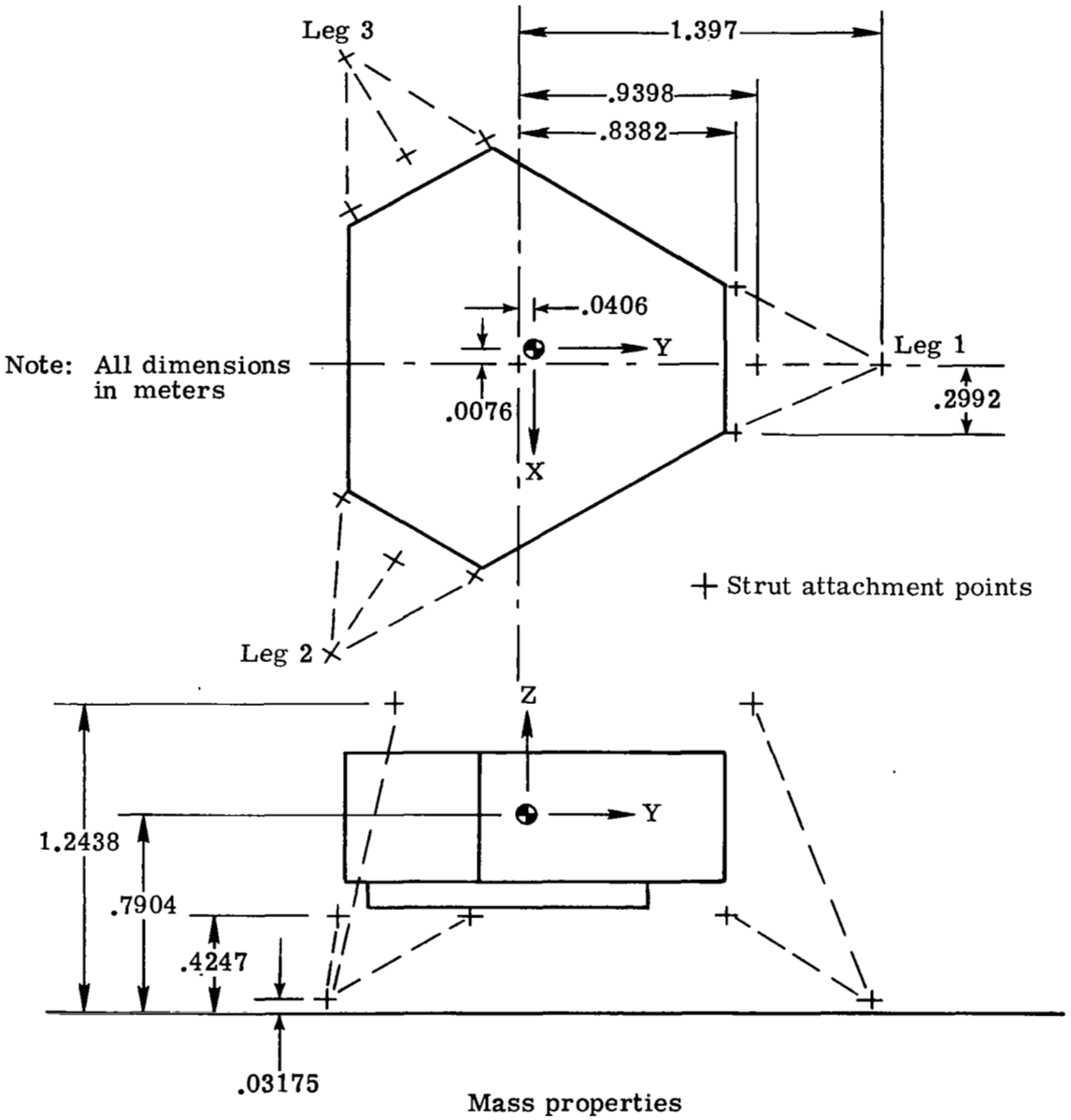

Mass properties

Weight - 575.8 kg

I_{XX} - 162.7 kg-m^2

I_{YY} - 216.9 kg-m^2

I_{ZZ} - 298.3 kg-m^2

Figure 3.- Viking lander geometry and mass characteristics.

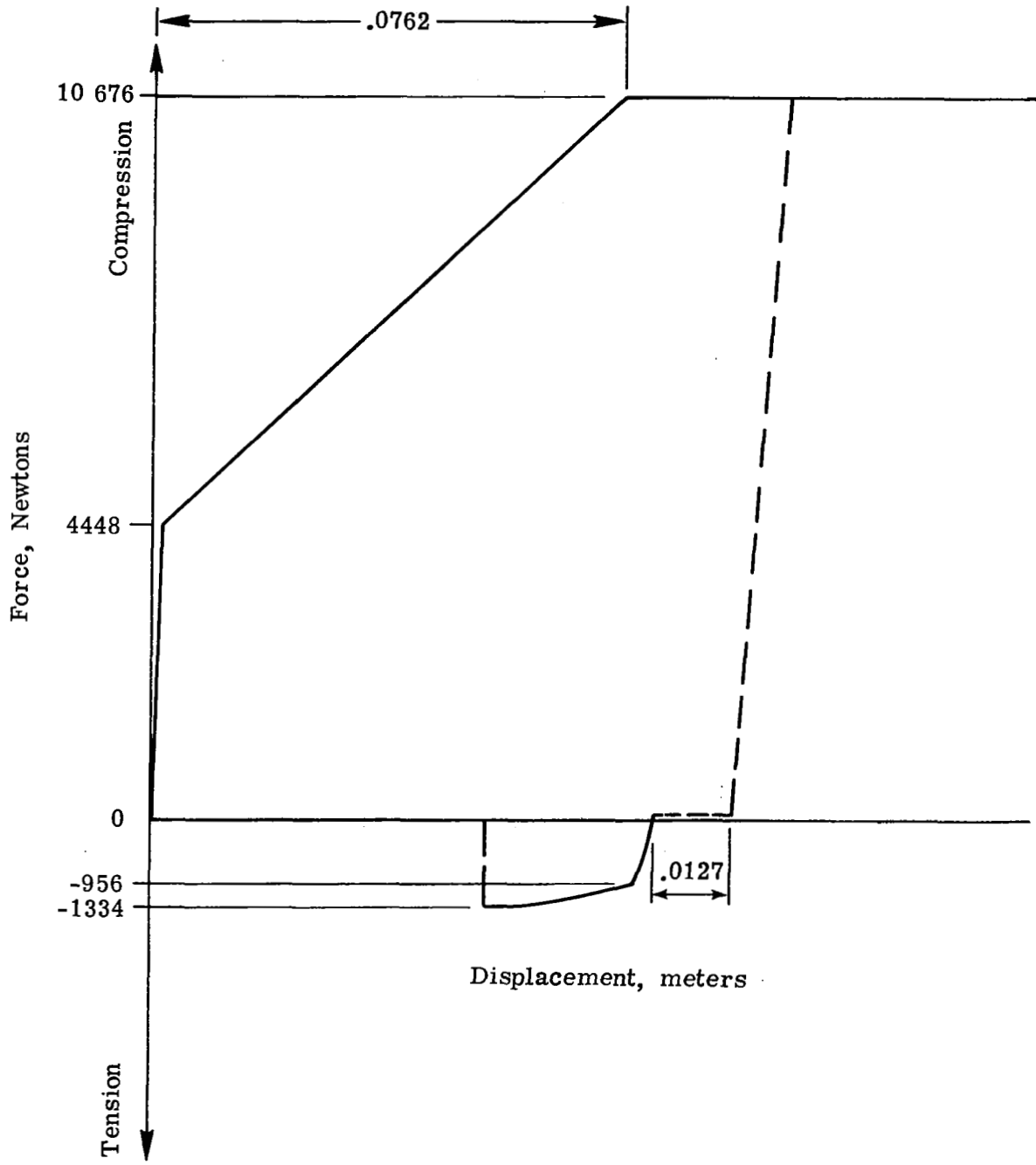

Figure 4.- Primary-strut load-stroke characteristics of Viking lander.

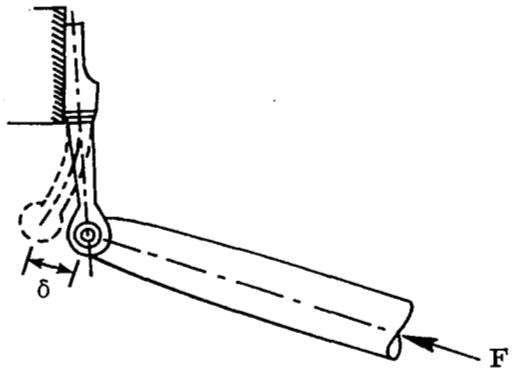

(a) Schematic drawing of secondary strut and limiter.

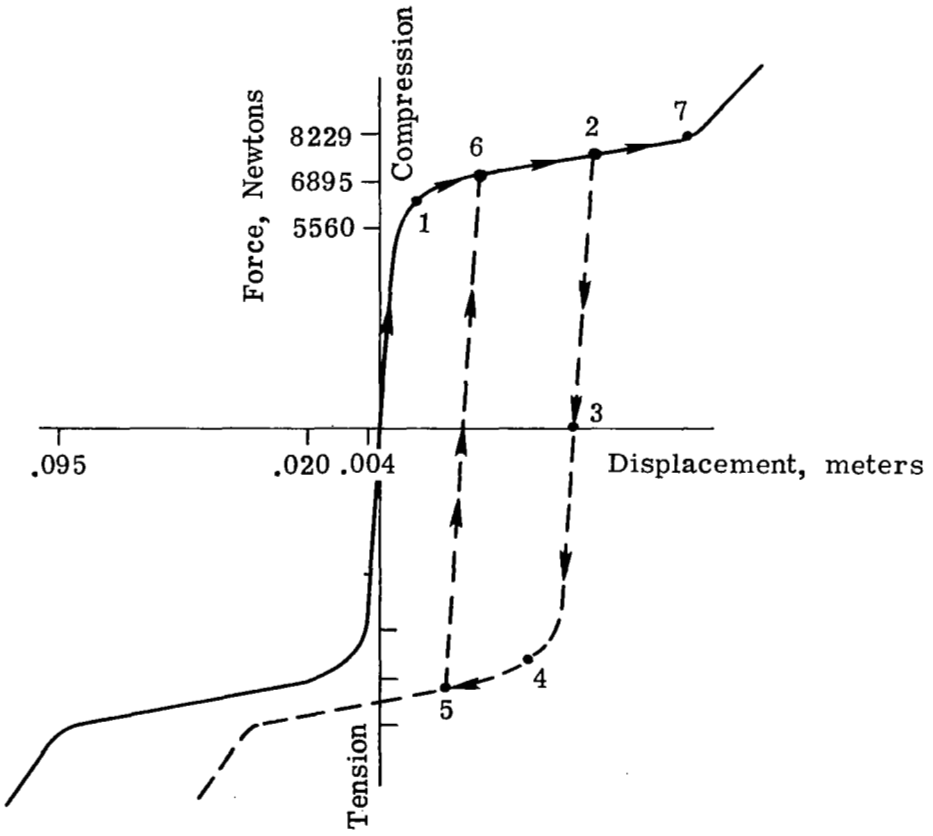

(b) Load-stroke characteristics.

Figure 5.- Schematic drawing of the Viking lander secondary strut and load limiter and their load-stroke characteristics.

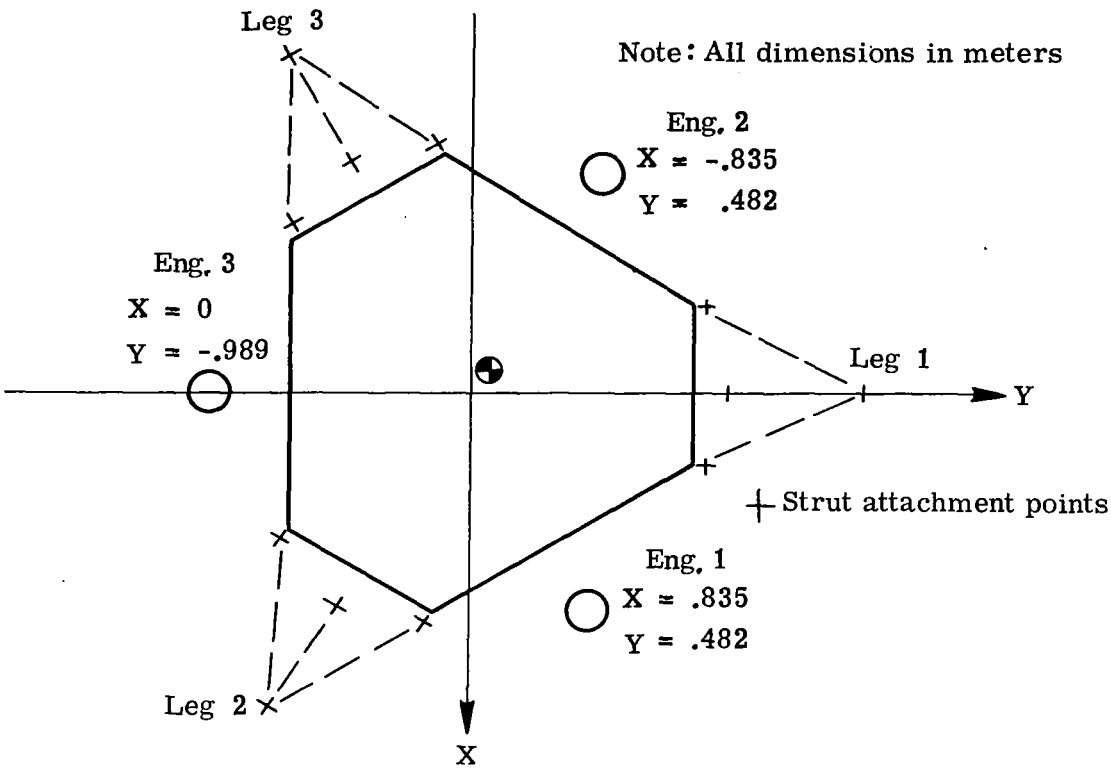

(a) Engine locations.

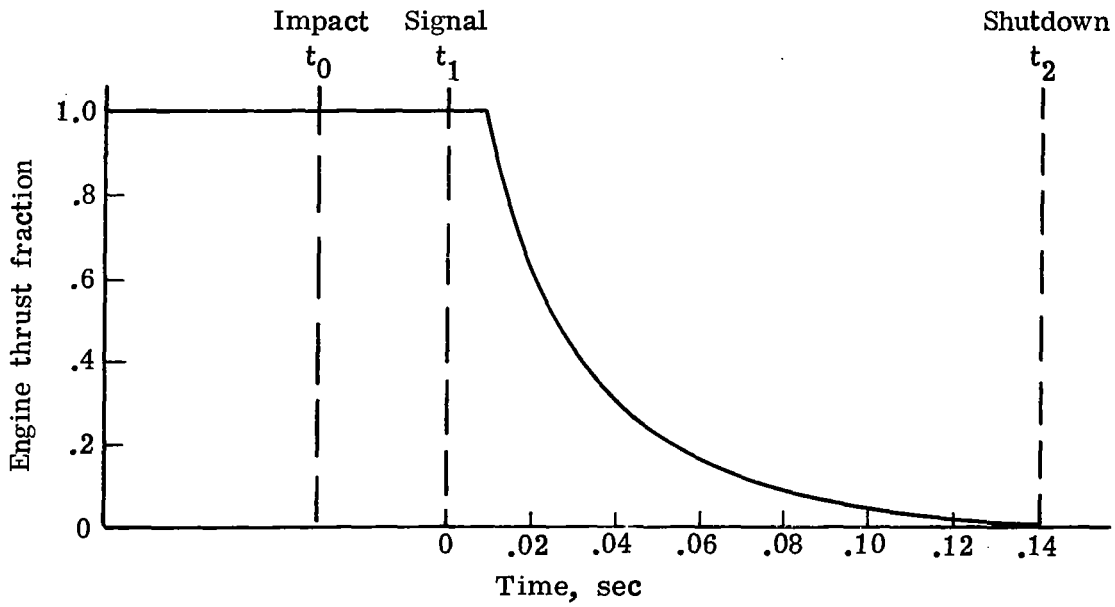

(b) Thrust tailoff characteristics.

Figure 6.- Engine locations and thrust tailoff characteristics for Viking lander.

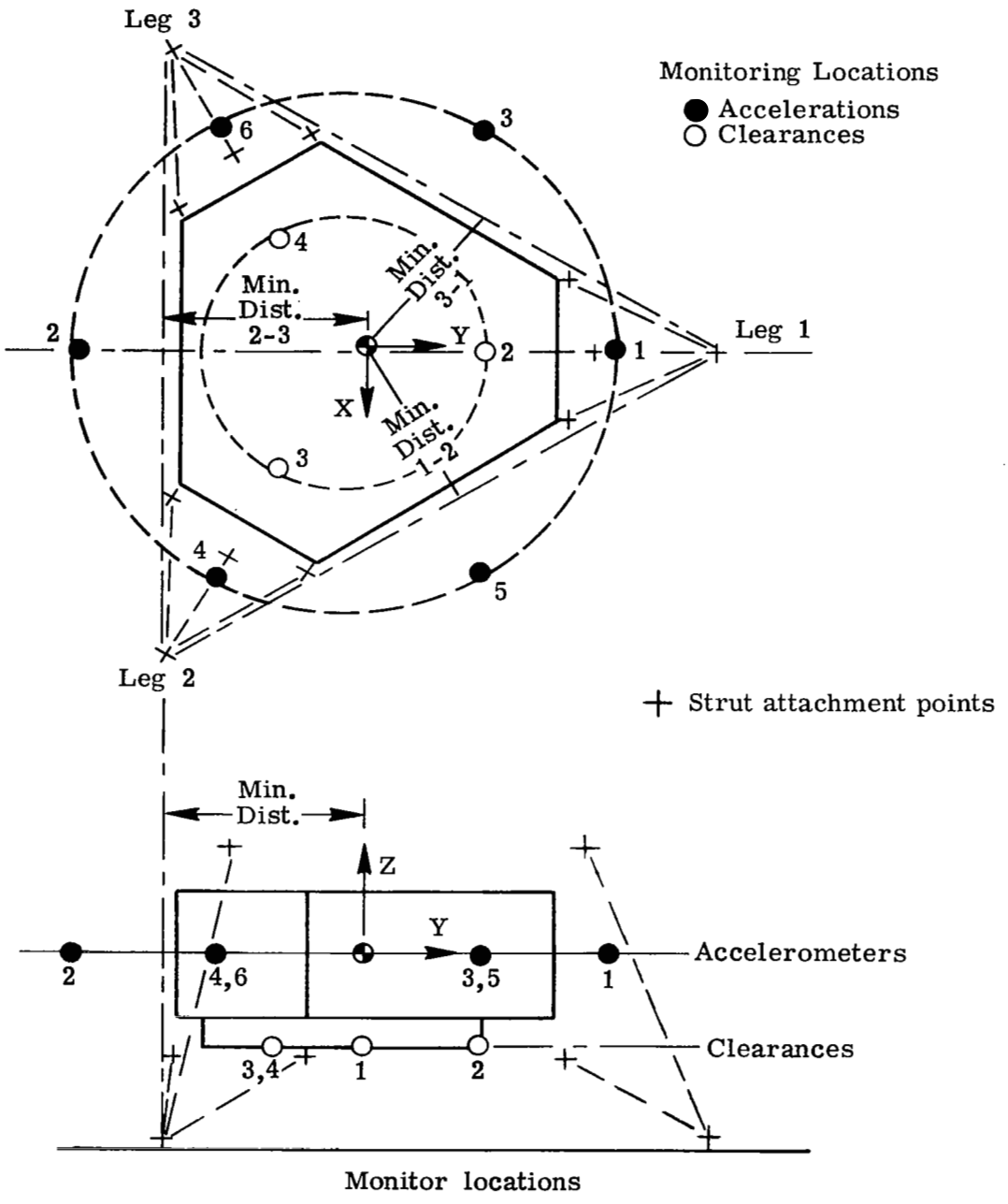

Figure 7.- Monitoring locations for stability, accelerations, and clearances for the Viking lander.

MEAN = 32.5 cm STANDARD DEVIATION = 1.04 cm

1st MOMENT $(\Sigma X_i / 100) = 3.250 \times 10^1$ cm

2nd MOMENT $(\Sigma X_i^2 / 100) = 1.057 \times 10^3$ cm^2

3rd MOMENT $(\Sigma X_i^3 / 100) = 3.446 \times 10^4$ cm^3

4th MOMENT $(\Sigma X_i^4 / 100) = 1.124 \times 10^6$ cm^4

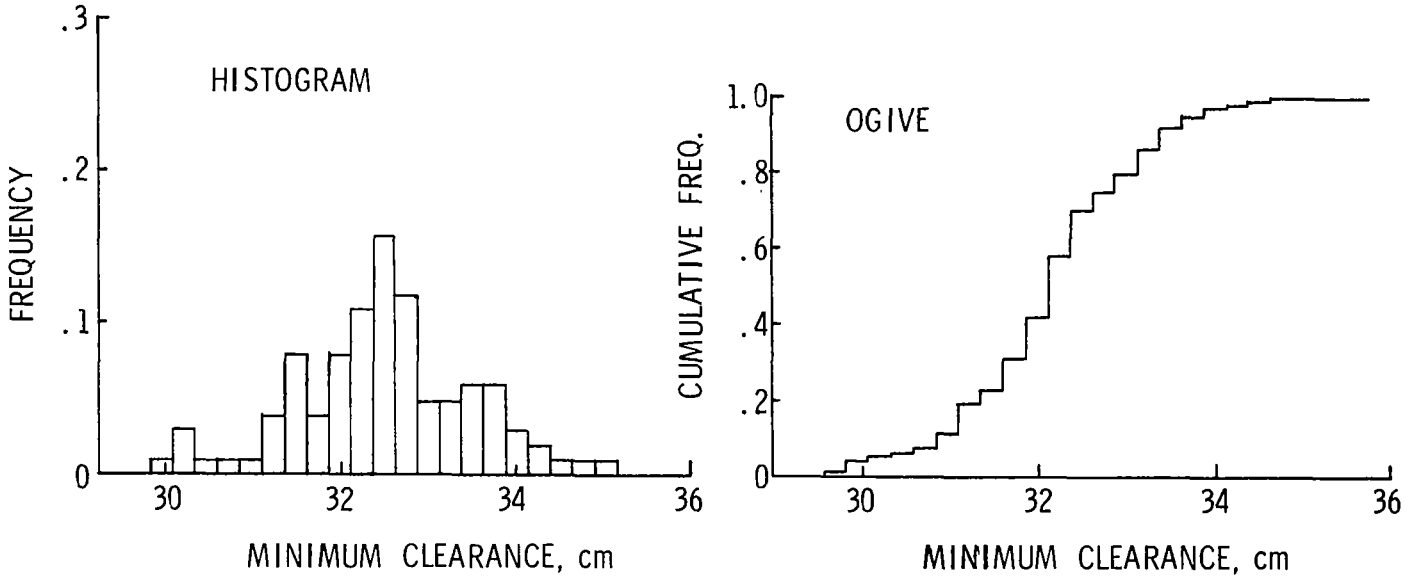

Figure 8.- Minimum-clearance statistics.

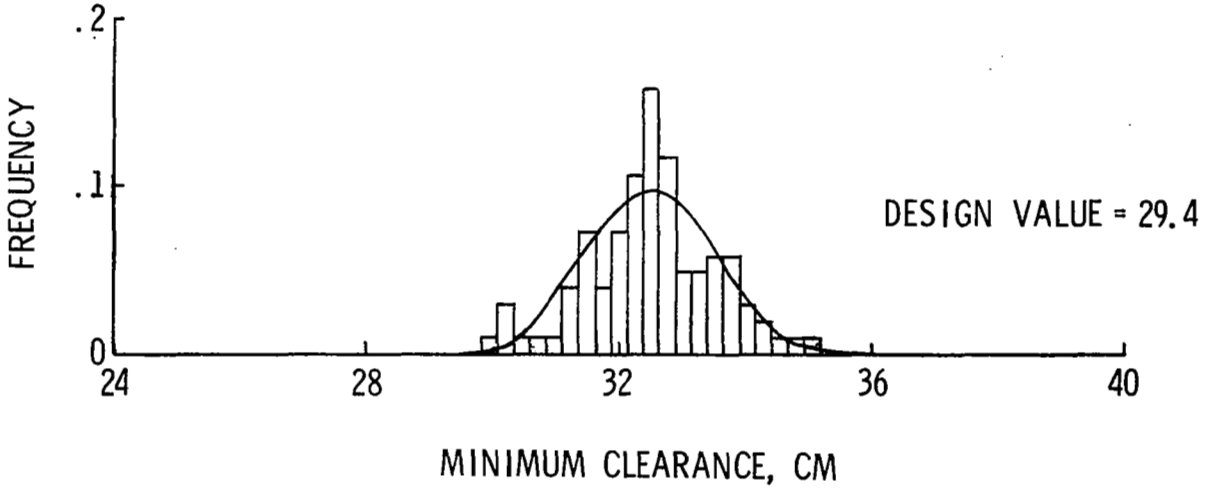

(a) Gaussian distribution (method 1).

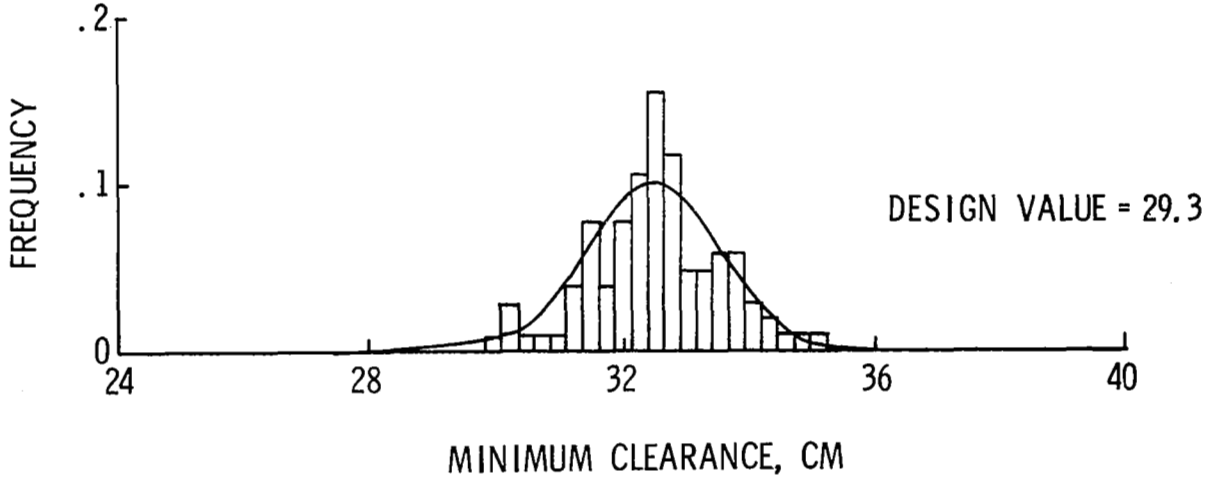

(b) Pearson type IV distribution.

Figure 9.- Comparison of Gaussian and Pearson curve fits for minimum-clearance statistics.

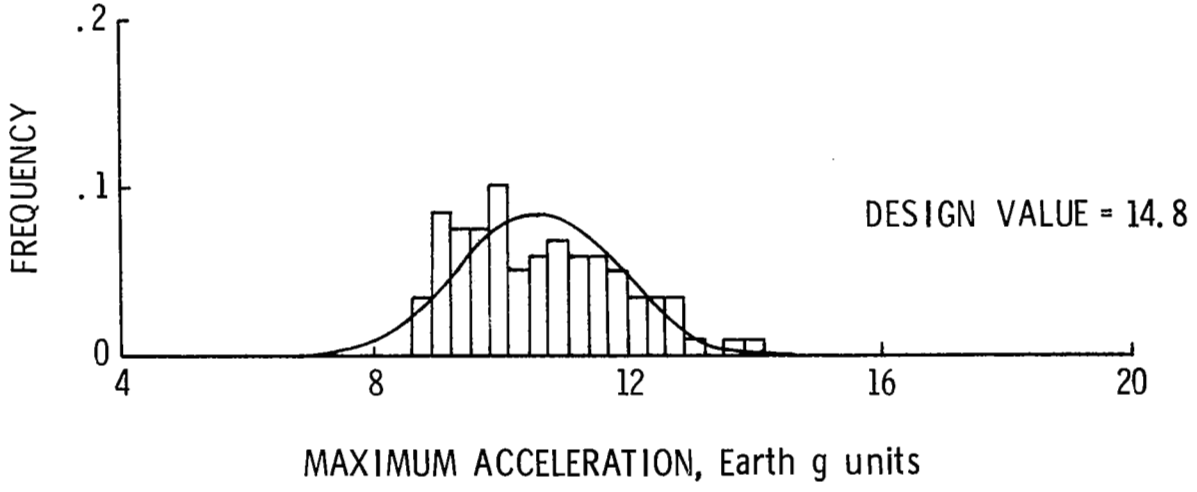

(a) Gaussian distribution (method 2).

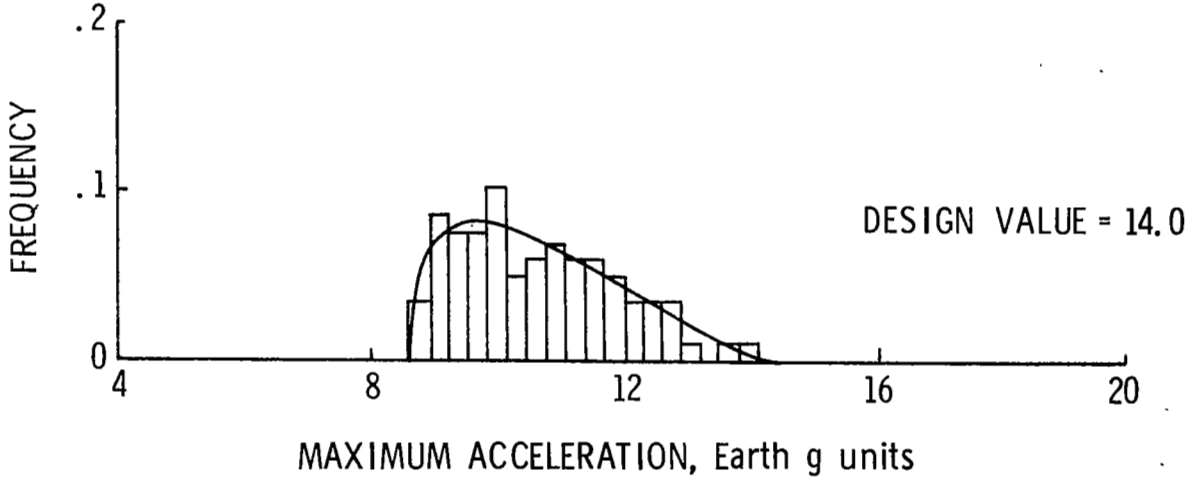

(b) Pearson type I distribution.

Figure 10.- Comparison of Gaussian and Pearson curve fits for maximum-acceleration statistics.

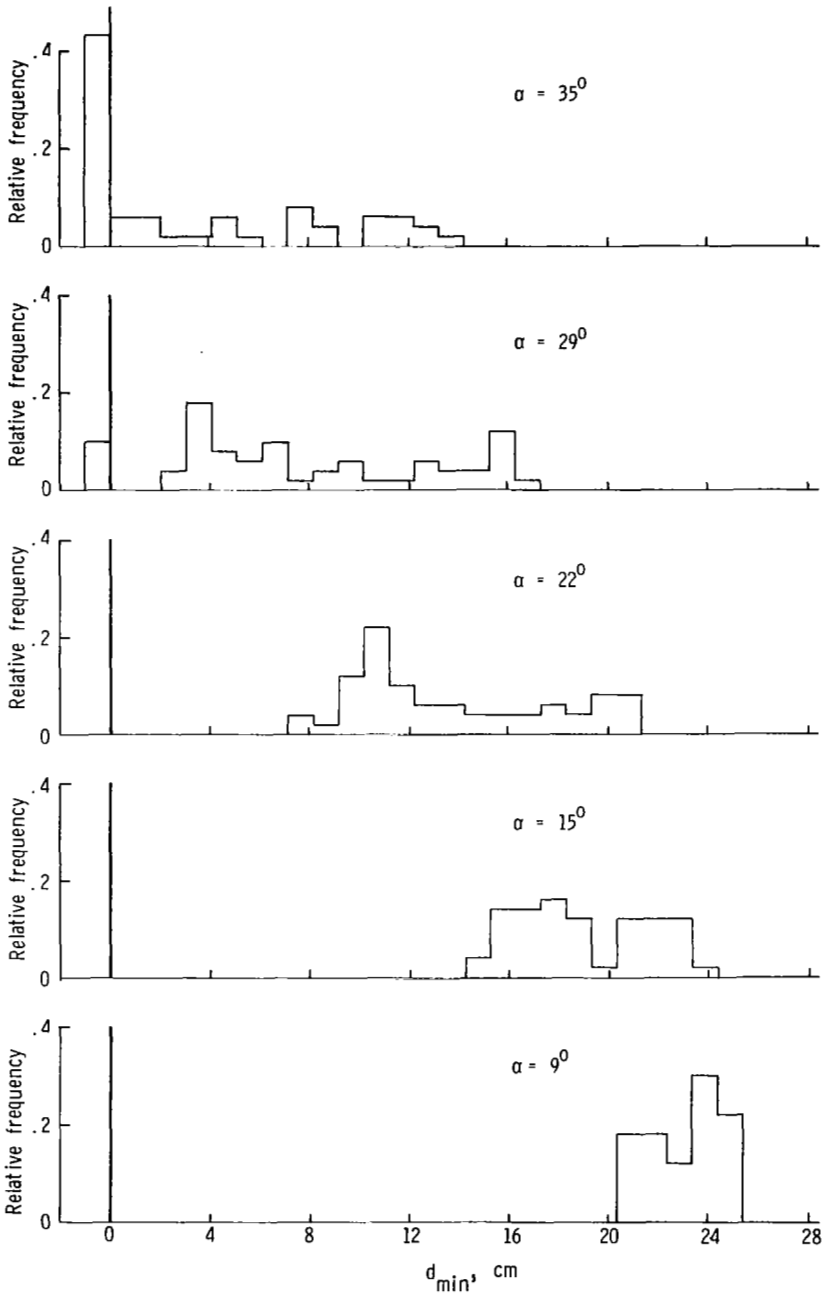

Figure 11.- Histograms of values of d_{min} for landings onto five discrete slopes.

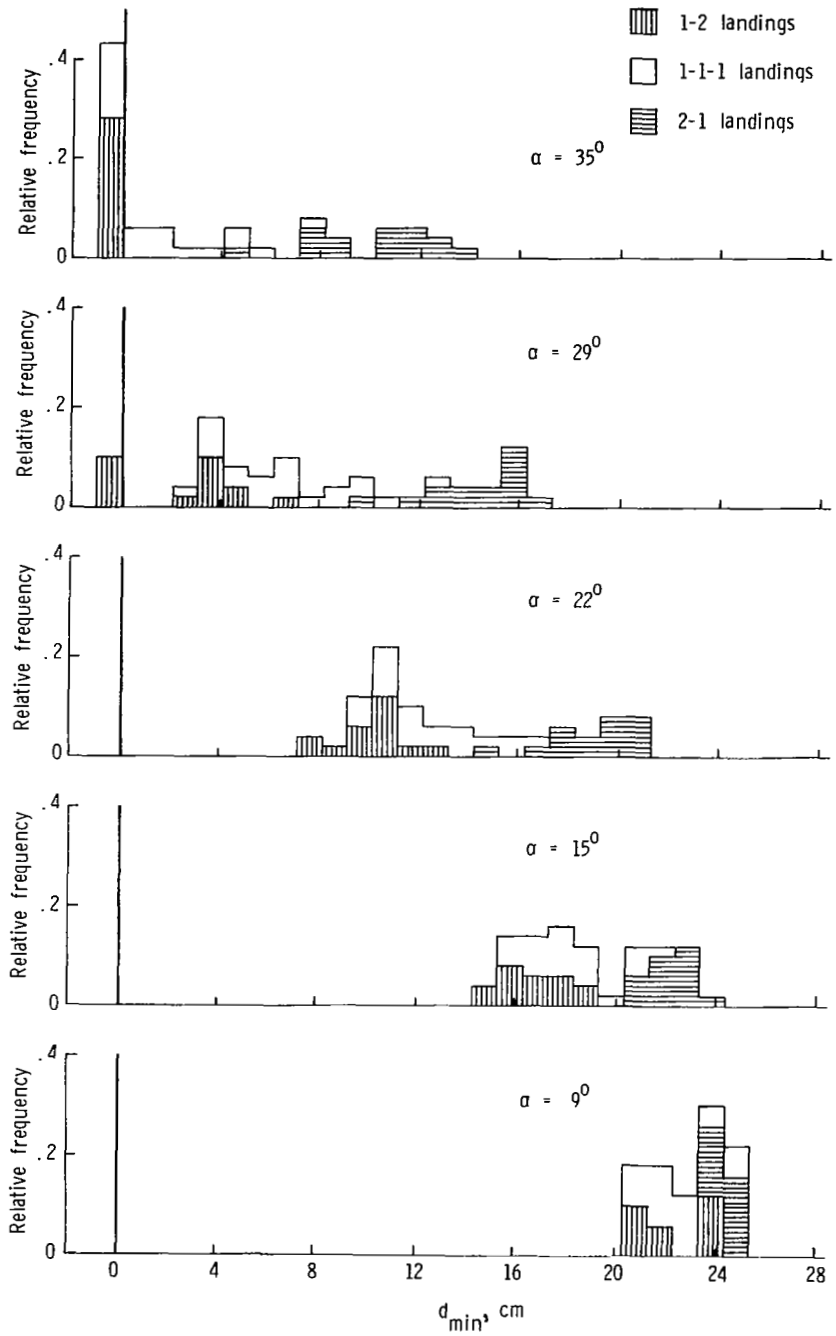

Figure 12.- Histograms of values of d_{min} showing the effect of leg-orientation categories.

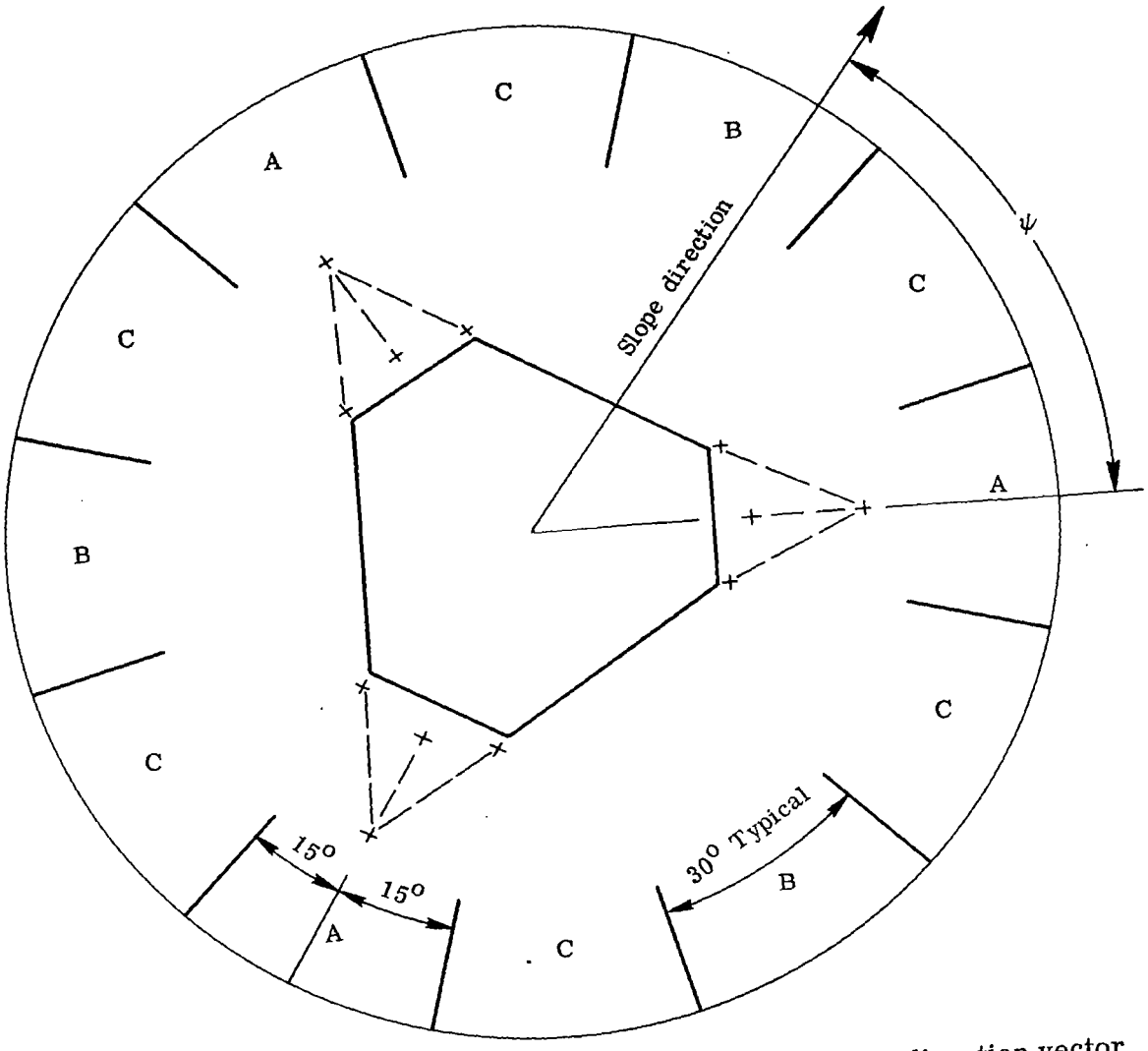

Figure 13.- Orientation of lander relative to surface-slope direction vector resulting in landing-category classification.

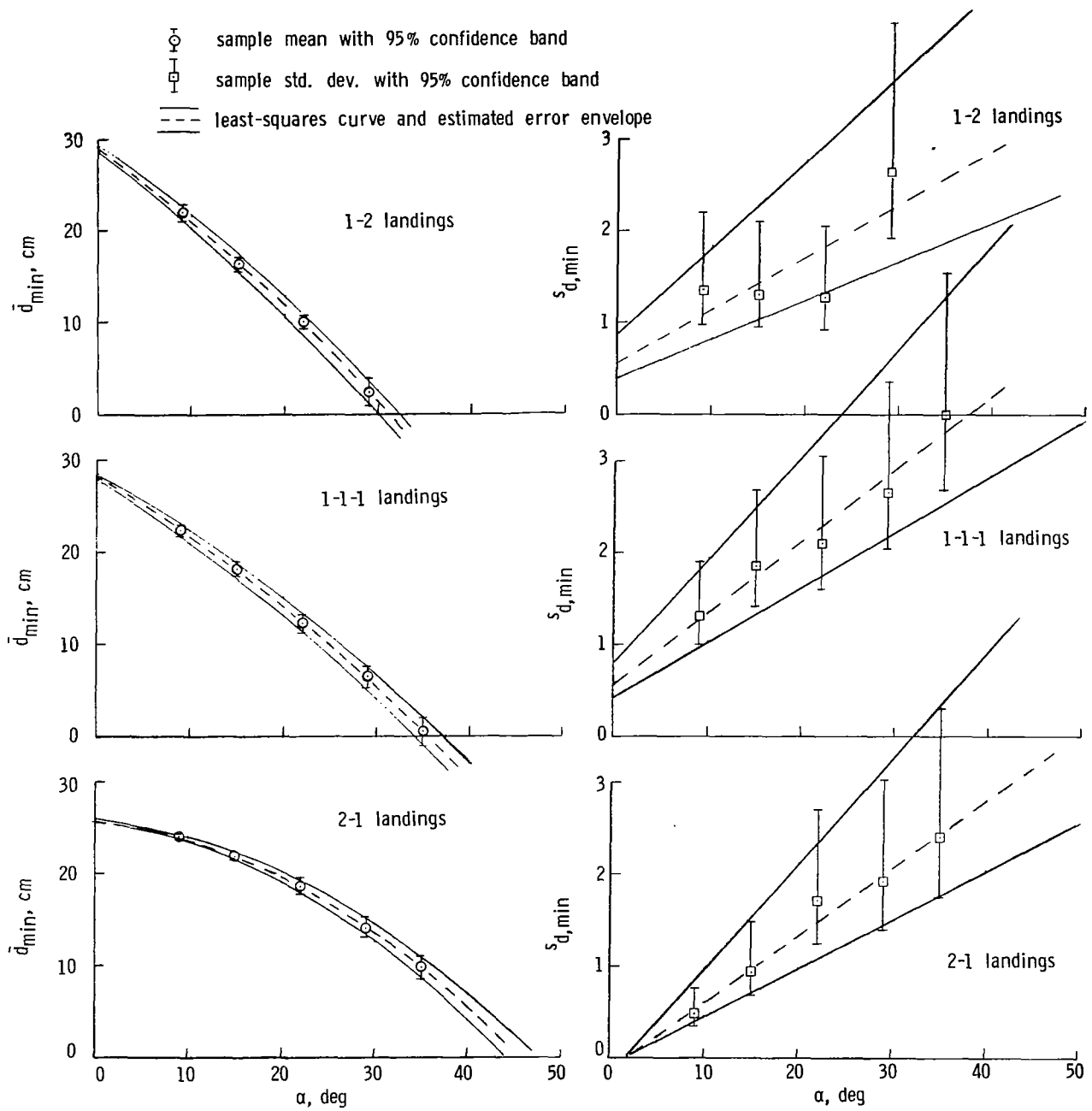

Figure 14.- Sample means and standard deviations of d_{min} as functions of surface slope.

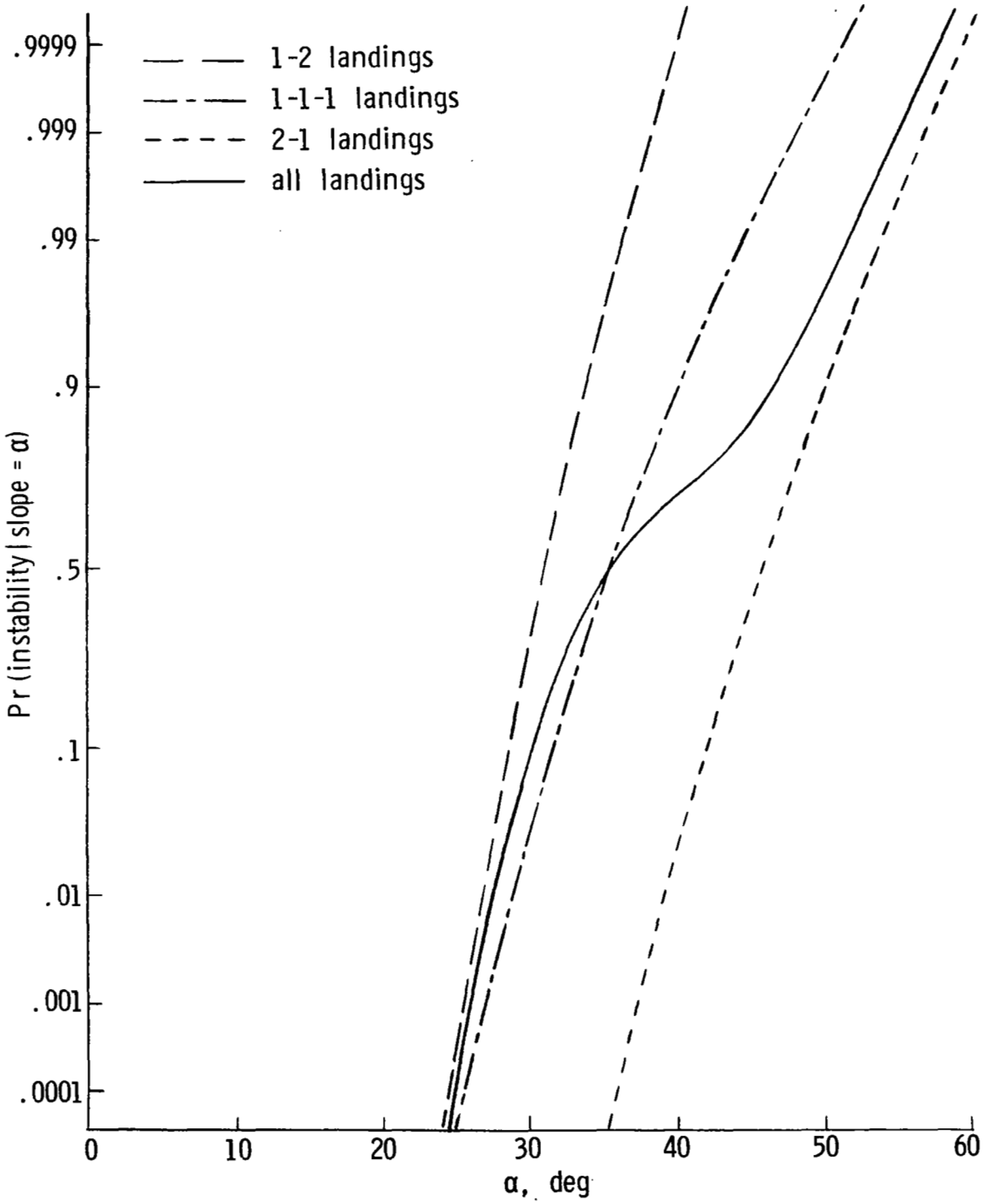

Figure 15.- Plot of $Pr(\text{Instability} \mid \text{Slope} = \alpha)$ against α for three landing types and for all landings.

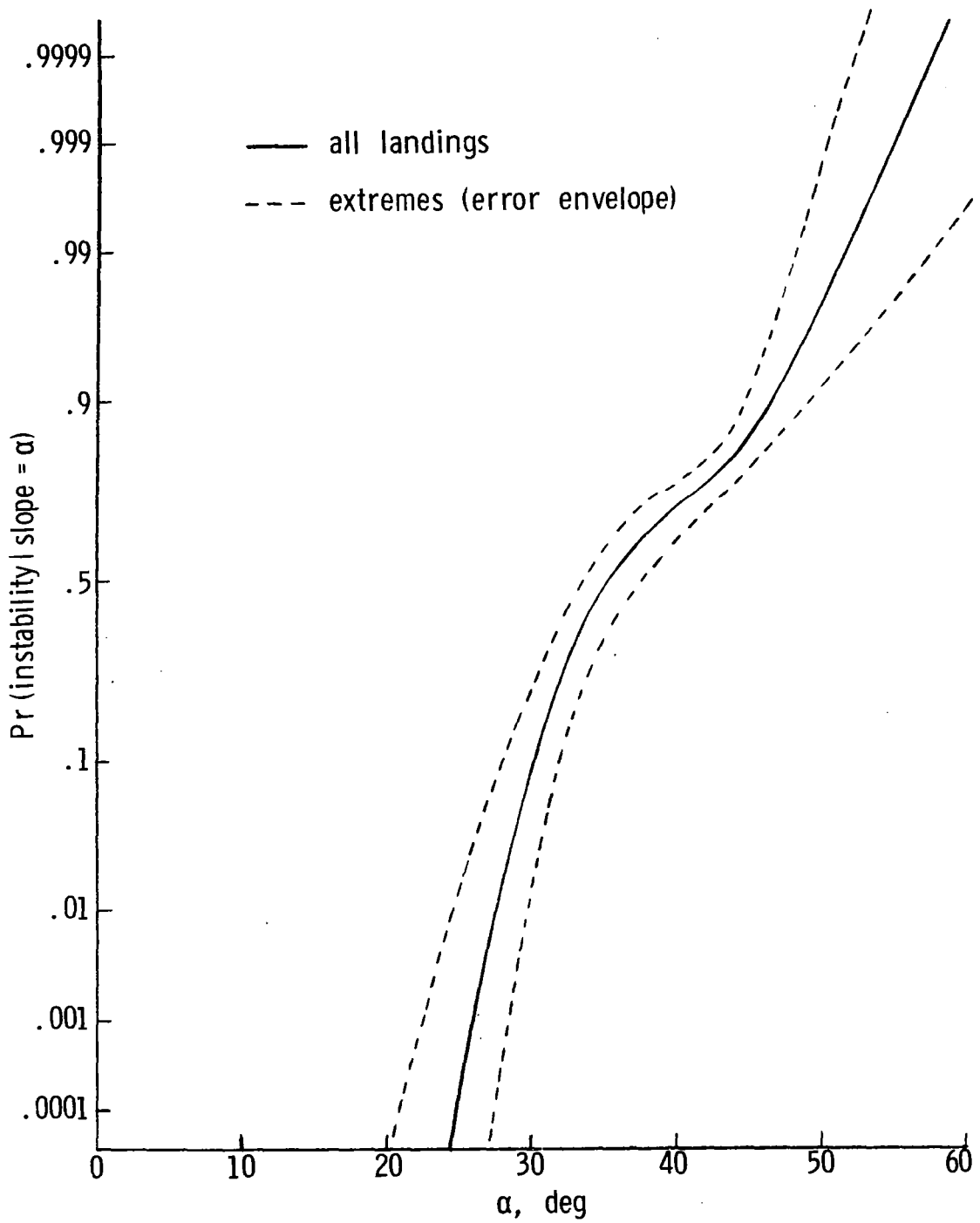

Figure 16.- Error envelope for the plot of $\Pr(\text{Instability} \mid \text{Slope} = \alpha)$ against α.

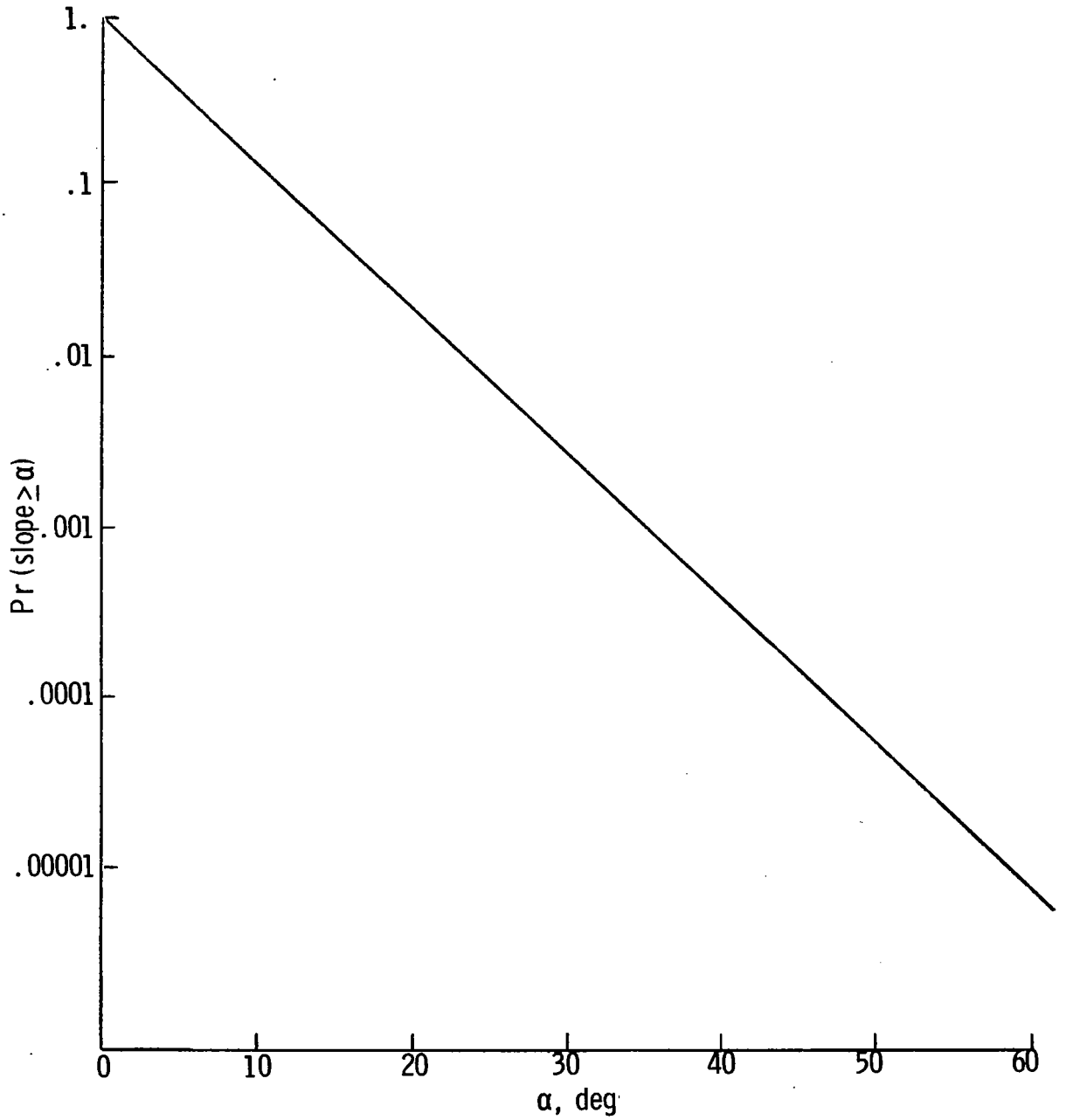

Figure 17.- Mars Engineering Model surface slope distribution.

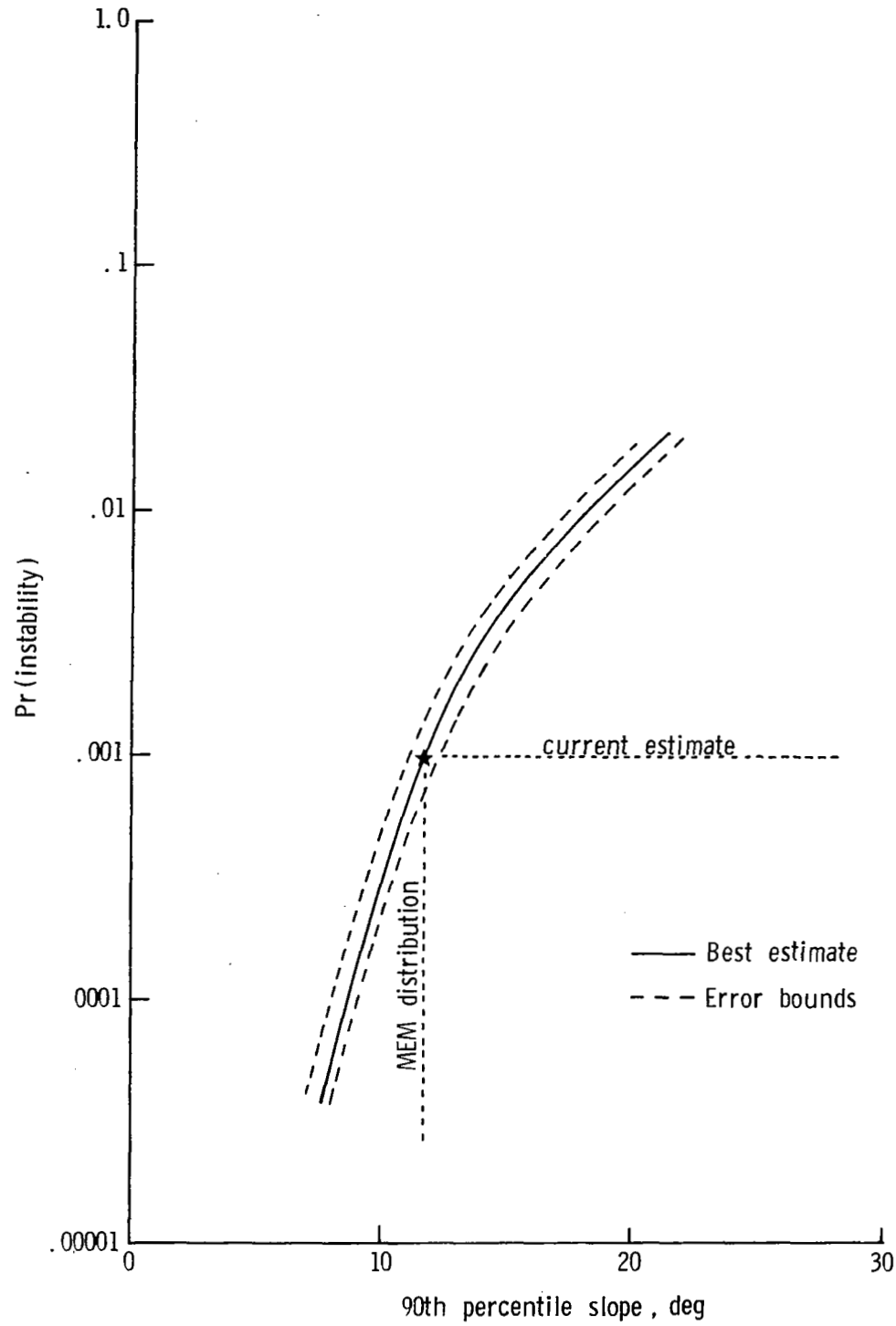

Figure 18.- Plot of Pr(Instability) against the 90th percentile slope.

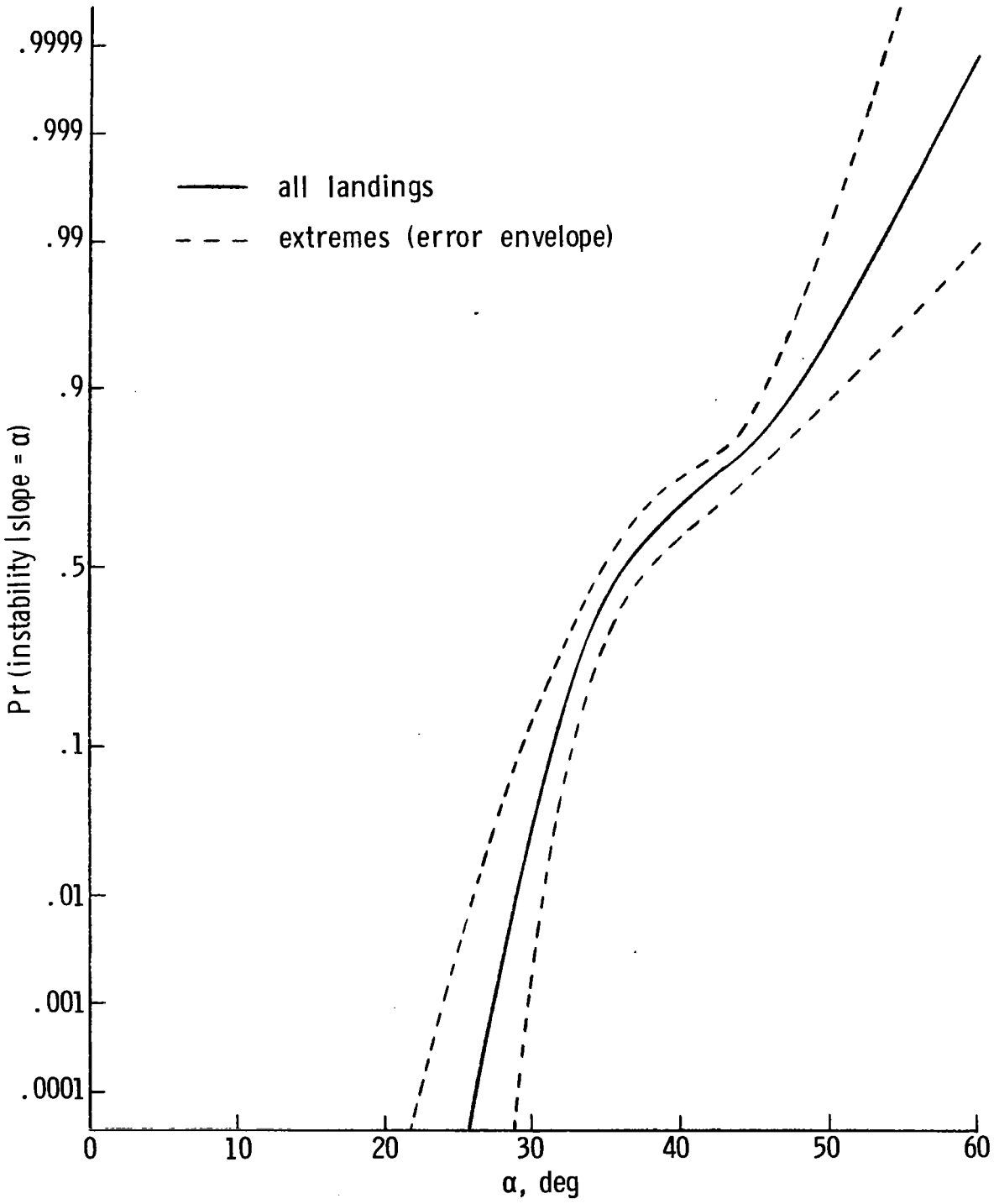

Figure 19.- Plot of $\Pr(\text{Instability} \mid \text{Slope} = \alpha)$ against α for the lander with ratchet.

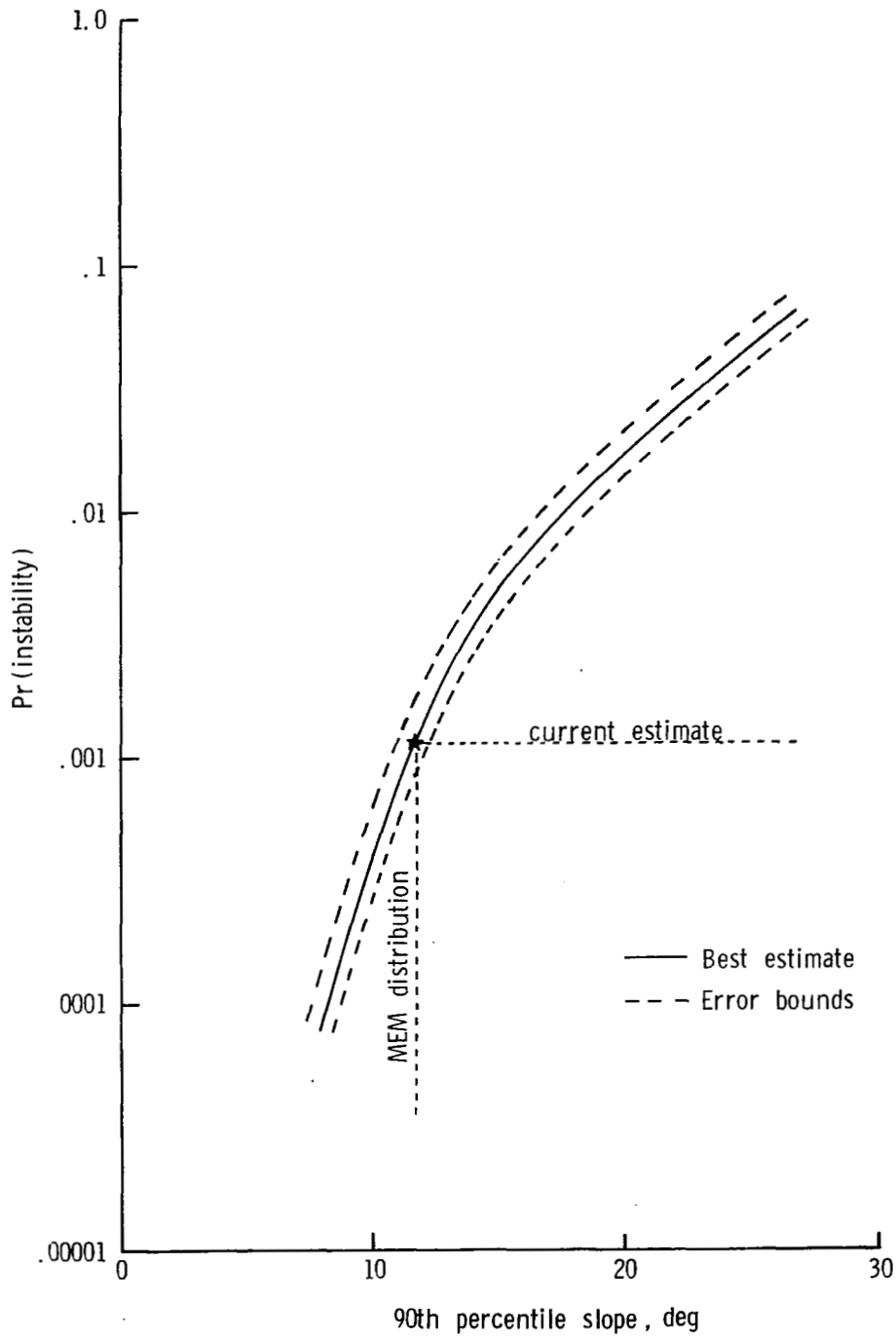

Figure 20.- Plot of Pr(Instability) against 90th percentile slope for the lander with ratchet.

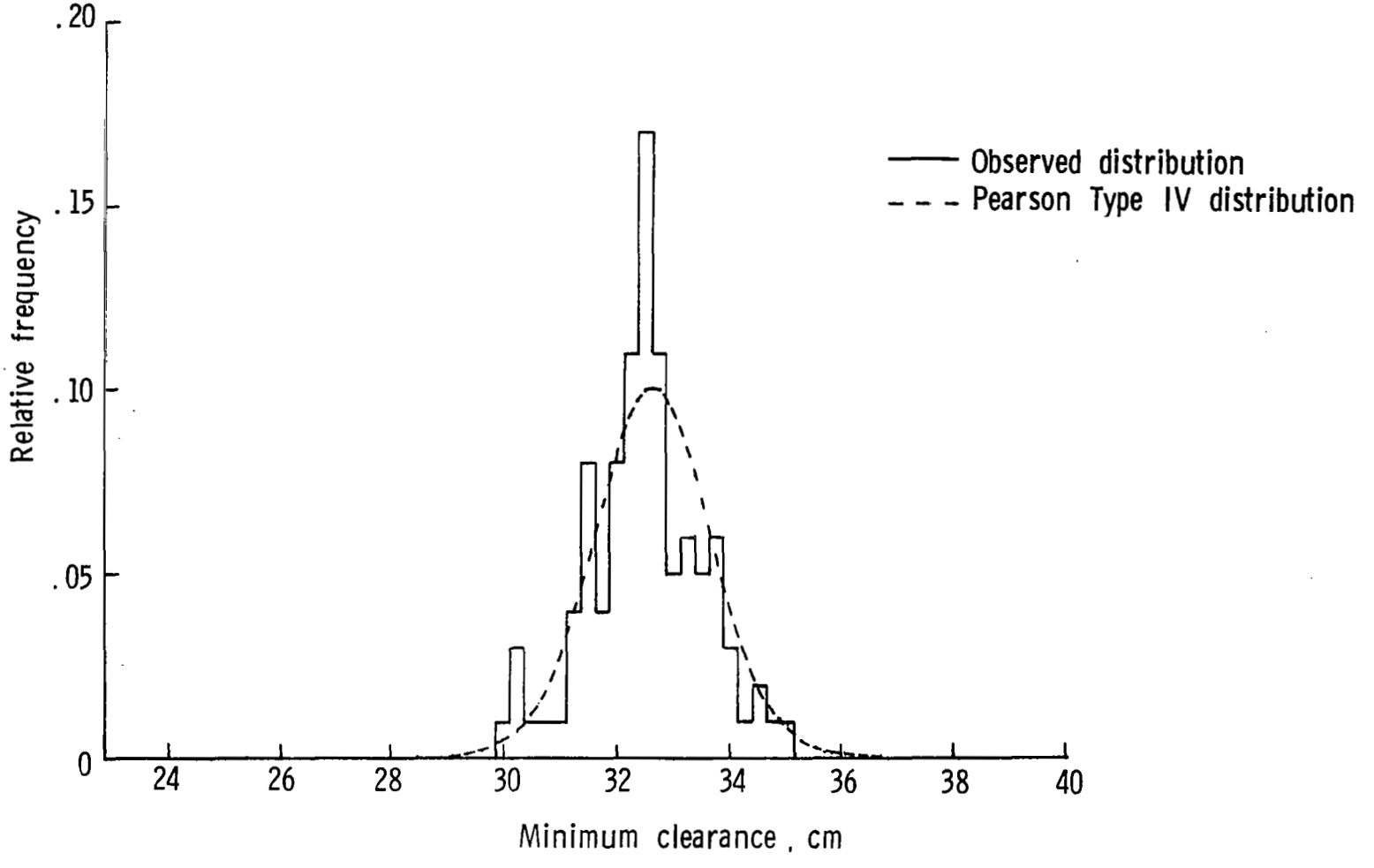

Figure 21.- Minimum-clearance distribution obtained from Monte Carlo landings.

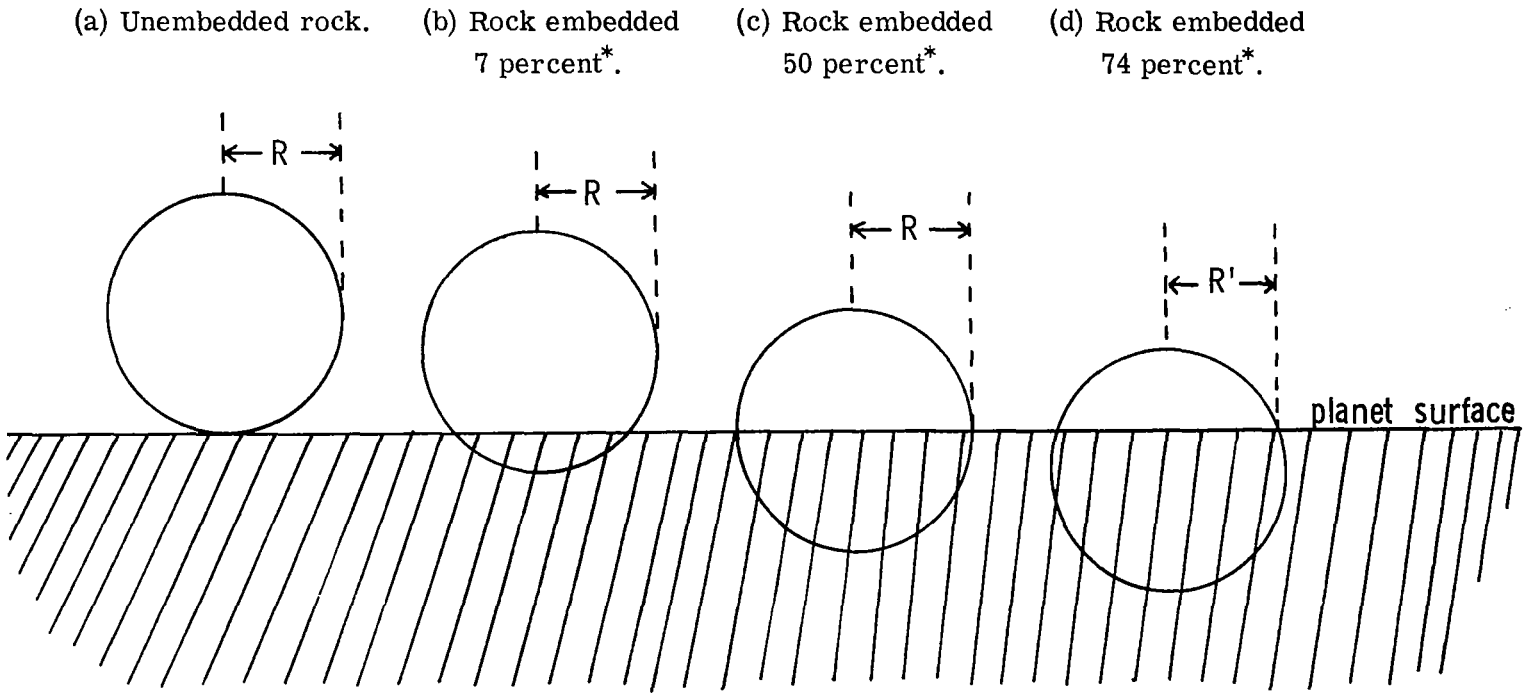

*percent embedded = percent rock volume below surface

Figure 22.- Rock model illustrating varying amounts of embedding.

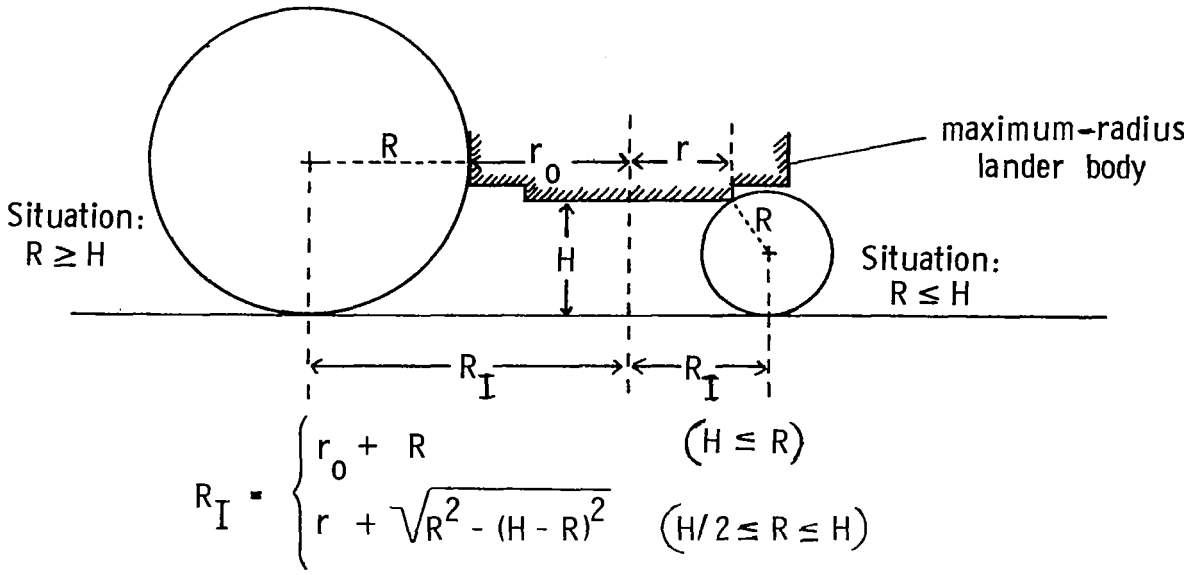

(a) Unembedded rocks.

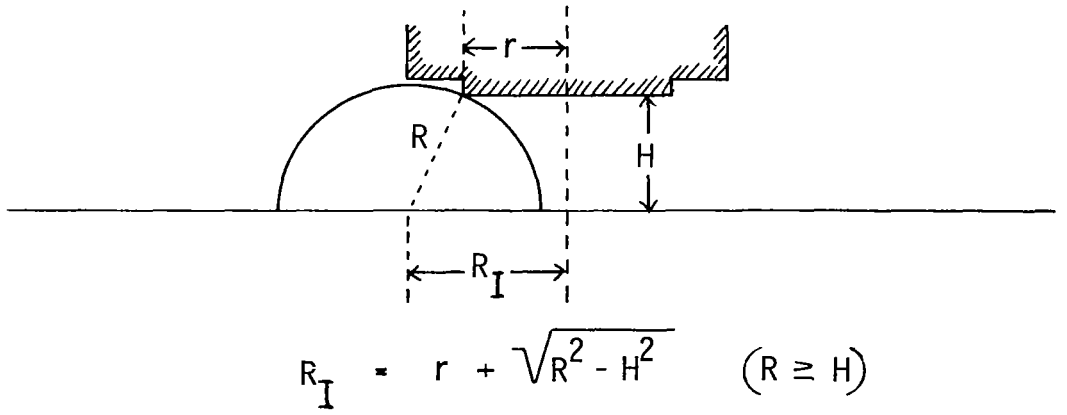

(b) Rocks embedded 50 percent.

Figure 23.- Diagrams of impact areas for rocks of radius R.

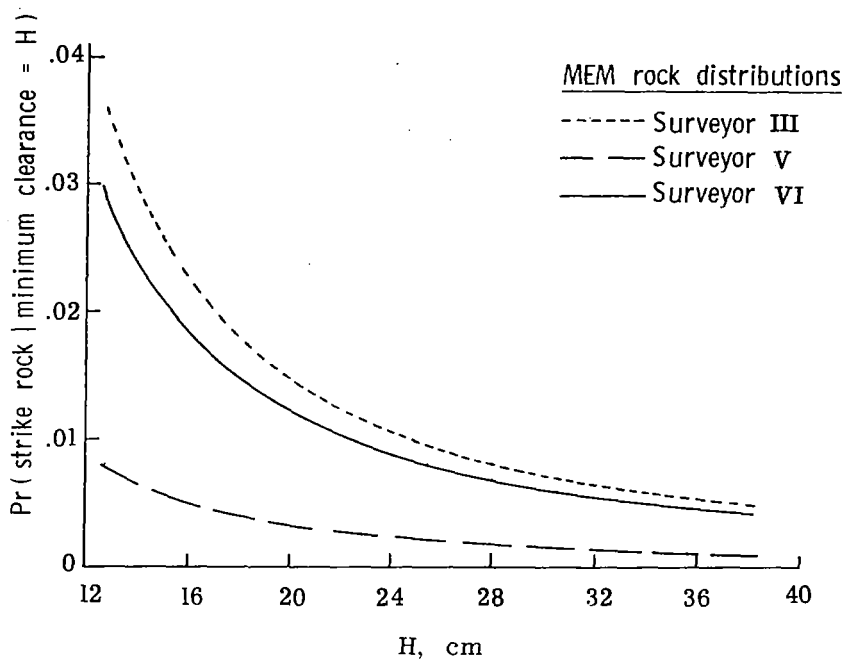

(a) Rocks embedded 50 percent.

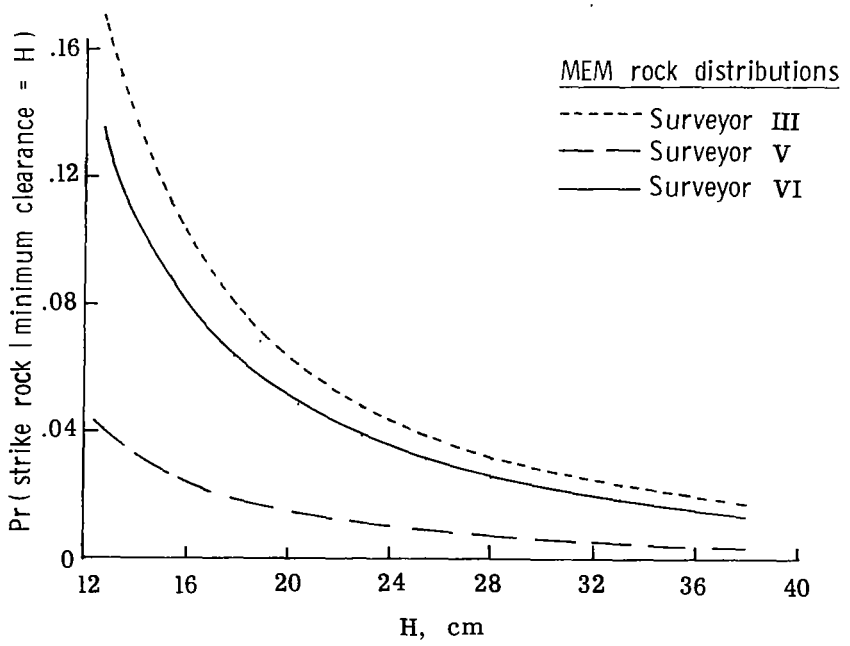

(b) Unembedded rocks.

Figure 24.- Plots of $Pr(\text{Strike rock} | \text{Minimum clearance} = H)$ against H.

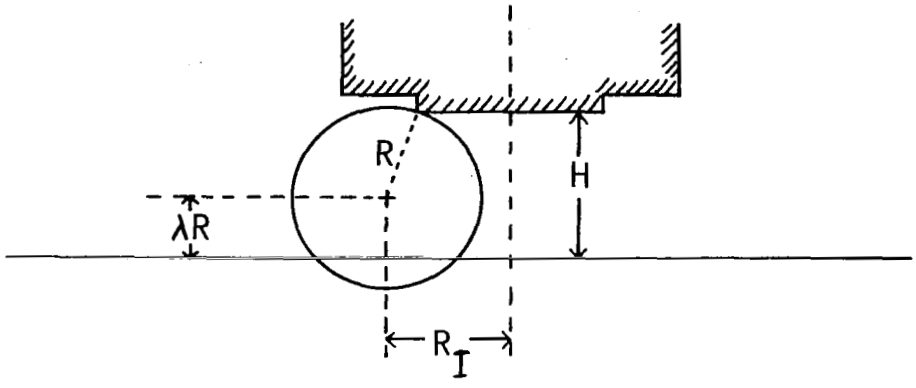

$$R_I = \begin{cases} r_0 + R & \left(H/\lambda \leq R\right) \\ r + \sqrt{R^2 - (H - \lambda R)^2} & \left(H/(\lambda+1) \leq R < H/\lambda\right) \end{cases}$$

Figure 25.- Diagram of generalized impact area for rock of radius R with embedding parameter λ.

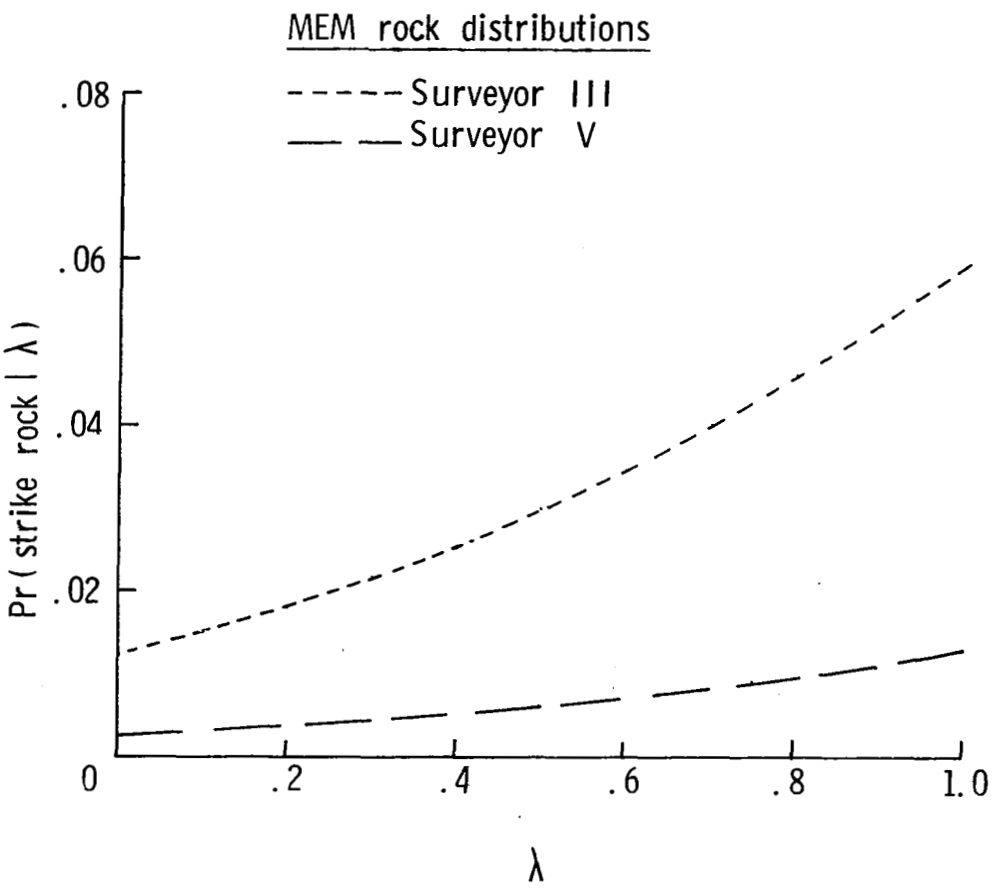

Figure 26.- Plot of $Pr(\text{Strike rock}|\lambda)$ against λ.

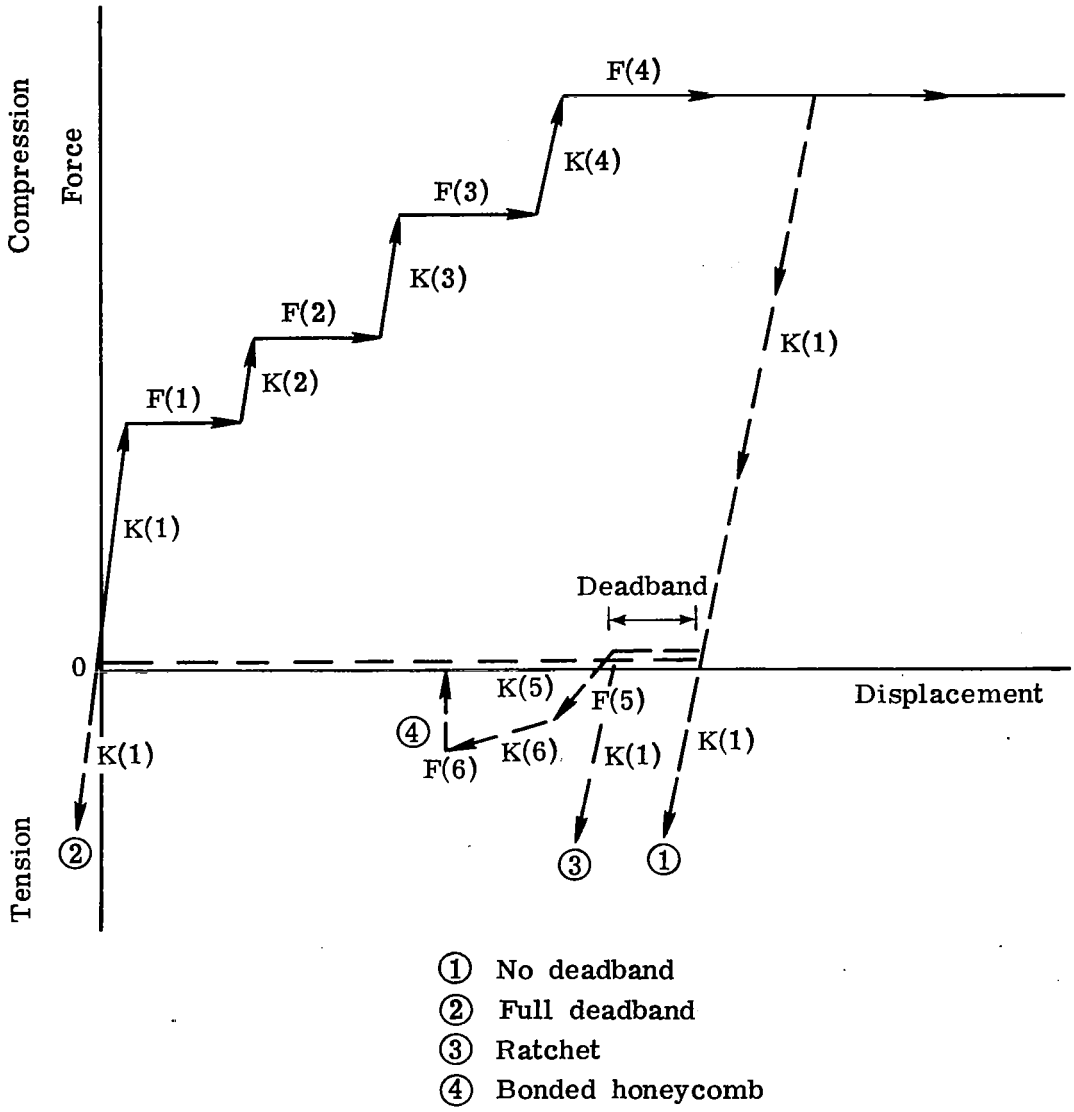

Figure 27.- Primary-strut load-stroke characteristics.

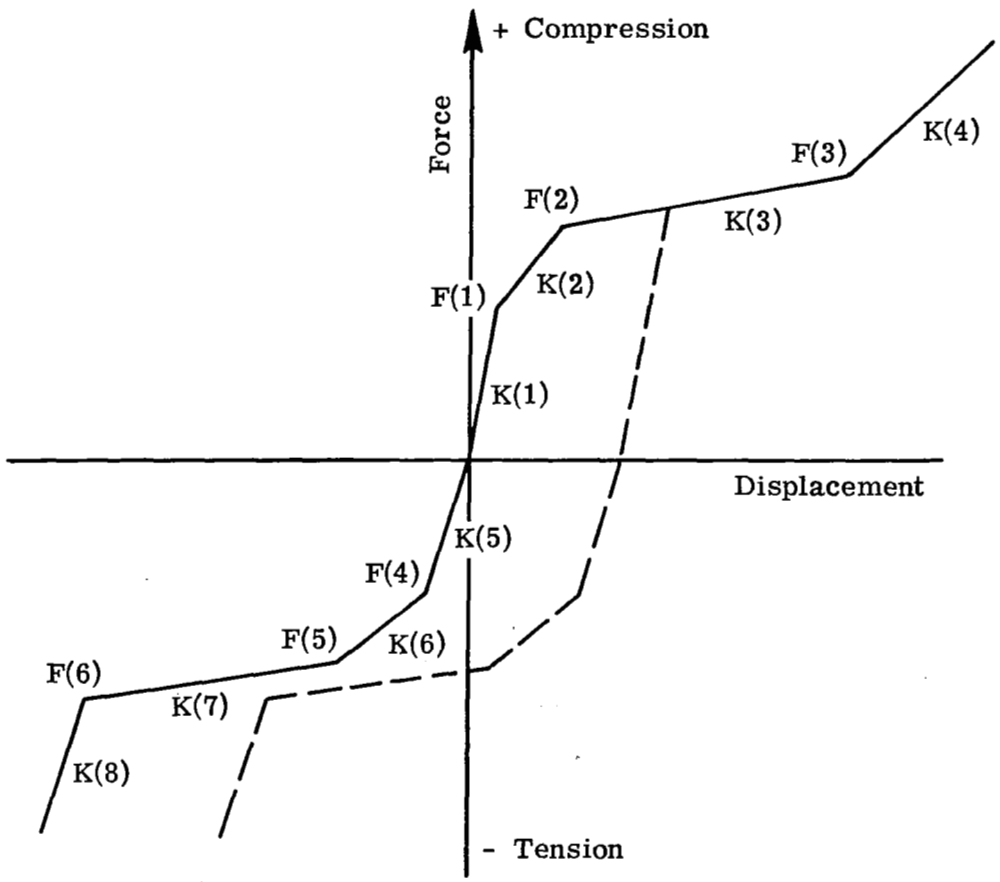

Figure 28.- Secondary-strut load-stroke characteristics.

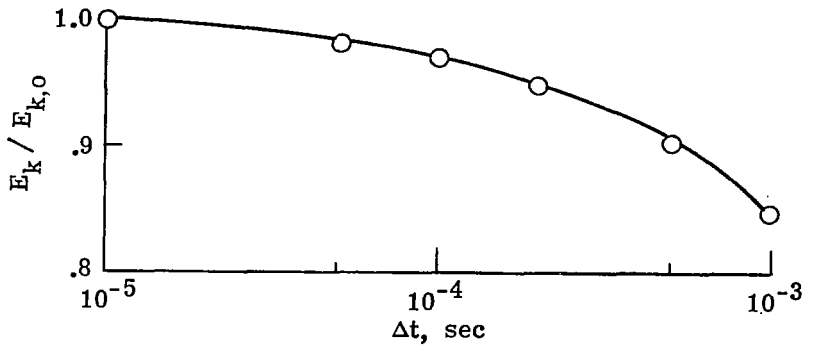

(a) Kinetic-energy ratio against time increment.

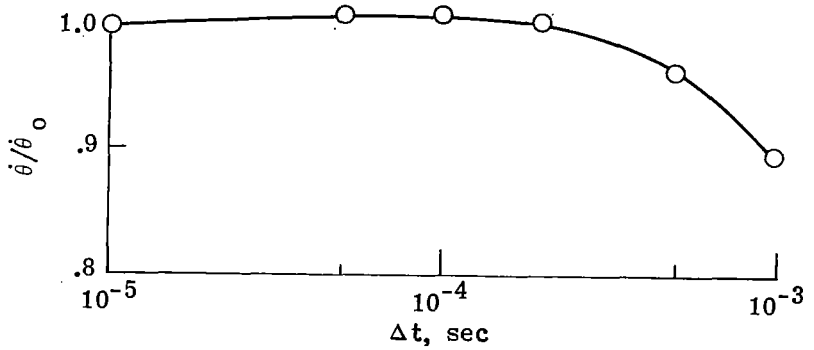

(b) Pitch-rate ratio against time increment.

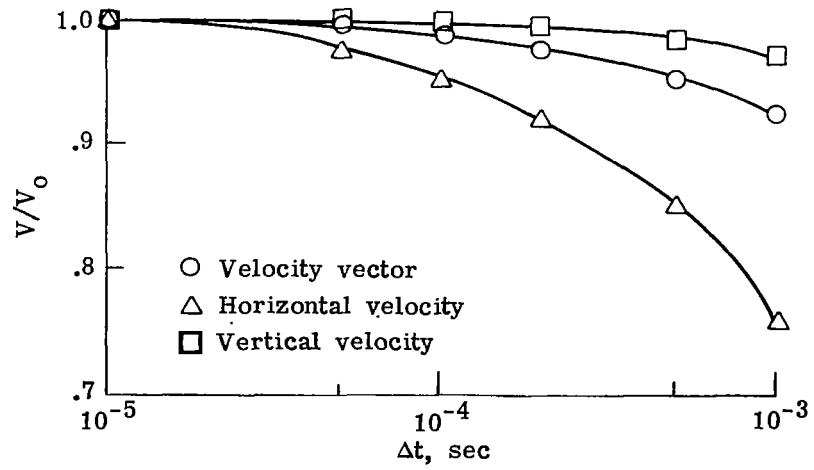

(c) Velocity ratio against time increment.

Figure 29.- Lander behavior plotted against time-increment size.